Multiscale microstructure and micromechanical properties of alkali-activated concrete: A critical review

Wenlin Tu, Mingzhong Zhang*

Department of Civil, Environmental and Geomatic Engineering, University College London, London, WC1E 6BT, UK

Abstract: With the rapid development of alkali-activated concrete (AAC) as a promising sustainable concrete, it is vital to thoroughly understand the microstructural characteristics and micromechanical properties, which determine the macroscopic mechanical properties and structural performance of AAC. This paper presents a critical review on the multiscale microstructure and micromechanical properties of AAC with both single and blend precursor systems, including alkali-activated fly ash (AAF), alkali-activated metakaolin (AAMK), alkali-activated slag (AAS), and alkali-activated fly ash-slag (AAFS). These types of AAC are systematically studied from nano-scale to macro-scale, covering solid gel particles (N-A-S-H, C-A-S-H and N-C-A-S-H), gel matrix (solid gel particles + gel pores), paste (unreacted particles + reaction products + pores), mortar and concrete (paste + interfacial transition zone + aggregates). The recent advances in microstructure and micromechanical properties of AAC are discussed, with special focus on microstructure-mechanical property relationships. The remaining challenges and opportunities for future research are also provided.

Keywords: Alkali-activated materials; Geopolymer; Reaction mechanisms; Phase assemblage; Interfacial transition zone; Nanoindentation

1. Introduction

As a promising alternative material to Portland cement (PC) concrete, alkali-activated concrete (AAC) has been demonstrated to achieve excellent mechanical properties and durability with environmental benefits [1-4]. In particular, the use of AAC can significantly contribute to reduction of CO_2 emissions while improving pollution levels and energy consumption compared to PC concrete [5-8]. The most commonly used precursors in AAC include fly ash, slag, metakaolin and their blends, which produce different types of AAC using alkaline solutions like sodium hydroxide (SH) and sodium silicate (SS) [9-12]. Alkali-activated fly ash (AAF) and alkali-activated metakaolin (AAMK) are considered as low-calcium AAC [12-15]. After dissolution of precursors and condensation reaction, alkaline aluminosilicate hydrates in a network structure are formed with the main reaction product of N-A-S-H gels [16, 17]. Alkali-activated slag (AAS) is regarded as high-calcium AAC, which undergoes the activation process with substitution of aluminium by silicate to form C-A-S-H gels [18, 19]. At ambient temperature, AAS exhibits excellent early-age mechanical performance, while AAF requires heat curing at around 60-90 °C for 24 h to achieve acceptable early-age comparative strength [20, 21].

* Corresponding author. E-mail address: mingzhong.zhang@ucl.ac.uk (M. Zhang)

However, AAF shows more superior fresh properties and suffers much less from strength reduction than AAS after exposure to elevated temperatures of up to 800 °C [3, 22-24]. Herein, the blended alkali-activated fly ash-slag (AAFS) has been introduced, which contains reaction products of N-A-S-H, C-A-S-H and N-C-A-S-H gels, to achieve desirable fresh and mechanical properties at ambient curing temperature [25].

To promote the engineering applications of different types of AAC, the mechanical properties and structural performance of AAC have been extensively examined over the last two decades. Based on recent advances, the engineering properties (e.g., fresh and mechanical properties) of AAC are systematically reviewed in several studies, mainly focusing on the factors that affect the mechanical properties of AAC such as precursor type, activator nature, curing conditions, additives and fibre content [6, 26-28]. Besides, a few attempts have been made to review microstructural characteristics of AAC, providing some information on chemical compositions, reaction kinetics, phase assemblage, morphology and pore structure of AAC under different curing conditions [29-31]. These microstructural characteristics are closely related to the macroscopic mechanical properties of AAC, while the relationships between them have been rarely discussed [32]. The mechanical performance is significantly associated with the contribution of micromechanical properties of different individual phases in AAC, such as elastic modulus that relates to stiffness, and hardness which represents mechanical strength of matrix [25, 33-35]. Regarding reaction products in AAC, the elastics moduli of different gels follow an order of N-A-S-H gels (11-20 GPa [33, 36-39]) < N-C-A-S-H gels (19-23 GPa [25]) < C-A-S-H gels (35-47 GPa [35, 40]). Up to now, the existing reviews mainly concentrate on either microstructural features or micromechanical properties of AAC, while a systematic review of the relationships between them from a multiscale point of view is still lacking.

This paper presents a critical review on the multiscale microstructural and micromechanical properties of different types of AAC. As per the continuum micromechanics, the complex heterogeneous structure of AAC can be classified into four different levels with multiple length scales [41-43], including Level 0: solid gel particle (1-10 nm), Level I: gel matrix (10 nm - 1 μm), Level II: paste (1 μm - 100 μm), and Level III mortar and concrete (> 100 μm). The outline of this review is presented in **Fig. 1**. The reaction mechanisms of different types of AAC are firstly introduced, followed by a comprehensive discussion on microstructure evolution and micromechanical properties development of AAC, from N-A-S-H, C-A-S-H and N-C-A-S-H solid gel particles at Level 0 to interfacial transition zone (ITZ), mortar and concrete at Level III. Afterwards, the relationships between microstructure and mechanical properties in AAC are analysed and discussed in depth.

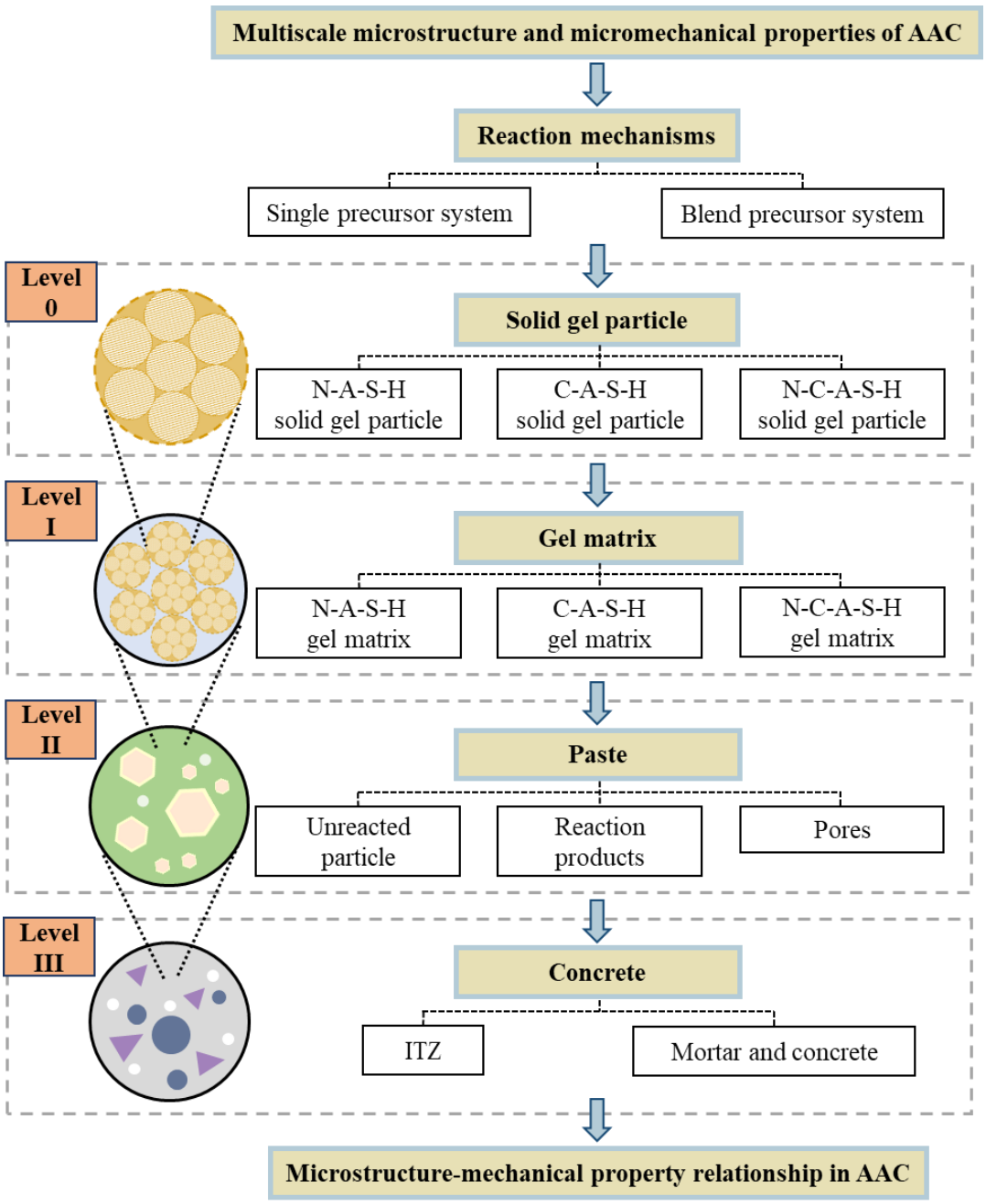

Fig. 1. Outline of this review.

2. Reaction mechanisms of AAC

2.1. Single precursor system

The identification of reaction products in AAC and relevant reaction mechanisms are mainly dependent on the calcium content in the system, which can determine the dominant types of gels within the matrix. The main reaction product in AAF and AAMK (low-calcium system) is an aluminosilicate-type gel, whereas calcium (alumino) silicate hydrate-type gel dominates the structure of AAS (high-calcium system) [2, 44]. The conceptual scheme for alkaline activation in the single precursor system is illustrated in **Fig. 2**. In general, the reaction process in both AAF and AAS can be divided into four steps: (a) dissolution, (b) rearrangement, (c) gel nucleation, and (d) solidification, hardening and strength development [2]. The reaction starts with the generation of a colloidal solution

of fine particles by the activation of alkaline solutions, followed by a combination into a continuous solid gel phase. Firstly, the dissolution of alumina and silica in precursors takes place under an alkaline environment composed of sodium/potassium hydroxides and silicates. The activation process disrupts the integrity of Si-O-Si and Al-O-Al bonds in fly ash, as well as Ca-O and Si-O-Si bonds in slag [43]. In consequence, different types of dissolved species are formed.

Afterwards, the formation of silica and alumino-silica dimers takes place, followed by trimers, tetramers and so on [43, 45, 46]. As the dissolution progresses, the rearrangement and exchange among dissolved species occur inside the structure, where the reaction of aluminium is more rapid than silicon at early stage of reaction due to a weaker bond in Al-O compared to Si-O [47]. Then, gel nucleation starts to take place with two main reaction products precipitated, consisting of cross-linked and disordered structures. In the low-calcium system with AAF, the sodium-alumina-silicate-hydrate (N-A-S-H) gels are formed, which tend to be Al-rich during early reaction process with an increase in the silicon concentration as time goes by. With the substitution of sodium by potassium, the potassium-alumina-silicate-hydrate (K-A-S-H) is also a common phase that forms in the low-calcium AAC. Due to the variations in the solvated ionic radius and hydration enthalpy between K and Na, discrepancies in affinities for negatively charged surfaces can be found in these gels [48-50]. As for the high-calcium system with AAS, the calcium-alumina-silicate-hydrate (C-A-S-H) gels are the main reaction products [2, 43].

2.2. Blend precursor system

In terms of blend precursor system with AAFS, many studies have reported the possibility of chemical interactions within the precursors as the reaction goes on [43]. This indicates that the development of N-A-S-H and C-A-S-H gels is not independent with structural and compositional changes during the reaction process [51, 52]. Within AAFS, a proportion of Ca^{2+} are released during the dissolution of slag particles, which can potentially substitute Na^{+} or incorporate into N-A-S-H gels to form N-C-A-S-H gels, as shown in **Fig. 2**. The local co-existences and phase transformation among N-A-S-H, C-A-S-H and N-C-A-S-H gels were suggested in AAFS, owing to a heterogeneous chemical distribution in the matrix [43, 53].

The interaction mechanisms between the activation of different precursors have been proposed in different aspects. Firstly, the microstructural characteristics of reaction products can be modified after the inclusion of blend precursors. Compared with plain AAS, a change in lattice parameters of C-A-S-H gels is noticed after only a slight addition of fly ash [53]. On the other hand, the deceleration or acceleration on certain crystalline phases is revealed. The increase of slag addition can either depress or trigger the precipitation of zeolite-type phases, since the local formation of N-C-A-S-H from N-A-S-H gels enhances the degree of heterogeneity in amorphous phases that impedes zeolite crystallisation [53]. A further inclusion of calcium from slag can lead to phase transformation from

N-C-A-S-H to C-A-S-H gels, which possibly replace alkali by its superior affinity to silicon [52, 54]. Furthermore, the spatial heterogeneity can be a crucial factor, depending on the binder ratio, dissolution kinetics of unreacted particles and local aqueous environments [53]. Besides N-C-A-S-H, it is worth noting that the incorporation of Fe-rich precursors can modify the original layered C-A-S-H gels to form the C-F-A-S-H gel by the interaction between Fe^{3+} and Ca^{2+} and Si^{4+} species in AAC [55-57]. Depending on different Fe/Si and Ca/Si ratios, the gel structural of C-F-A-S-H can vary among hydroandradite (Fe/Si < 0.2), disordered gel (Fe/Si > 0.2) and layered C-(F)-A-S-H (Ca/Si > 1) [57].

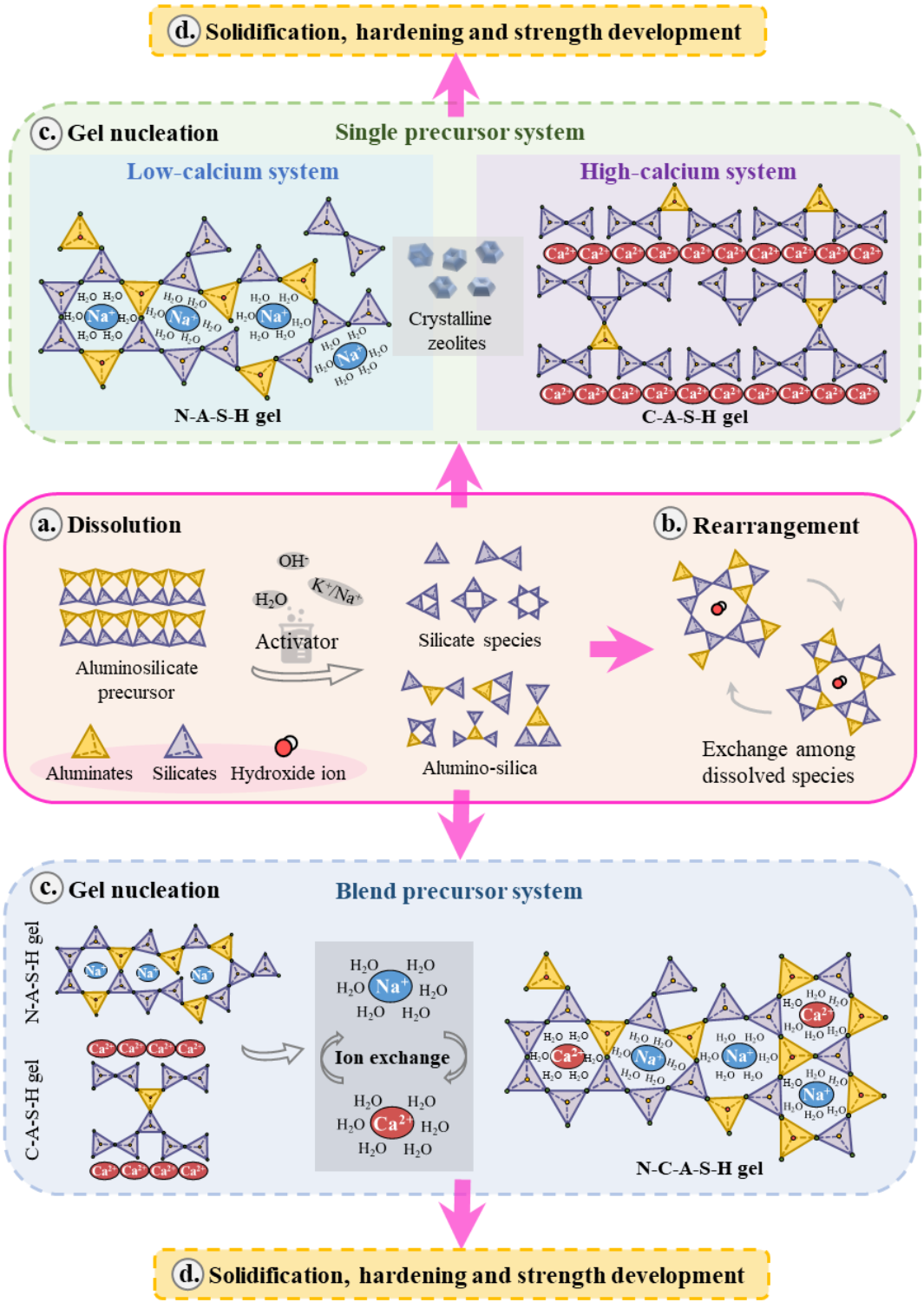

Fig. 2. Schematic diagram of the alkaline activation of low-calcium, high-calcium and blend precursors (Adapted from Refs. [2, 47, 58-60]).

3. Level 0: Solid gel particle

Level 0 delineates the nanoscale level, referring to the fundamental solid gel particle that serves as elementary component within the binder gel matrix [43, 53, 61]. The nanoscopic characterisation of three main types of solid gel particles (N-A-S-H, C-A-S-H and N-C-A-S-H) will be reviewed in this section with respect to microstructure and micromechanical properties.

3.1. N-A-S-H solid gel particle

3.1.1. Nanostructure

As the dominant reaction products in AAF and AAMK, N-A-S-H gels have highly cross-linked structures with SiO_4 and AlO_4 tetrahedra connected by shared O atoms, as illustrated in **Fig. 3(a)** [44]. The cross-links among chains provide sufficient cavities for the accommodation of alkali cations (Na^+), mitigating the charge deficiency resulting from the substitution of silica (Si^{4+}) with aluminium (Al^{3+}). N-A-S-H gels consist of a significant amount of Q^4(mAl) sites that are present in 3D networks with a silicon tetrahedron connecting to three other tetrahedrons. At the start of activation process, the formation of N-A-S-H gels is initiated by an Al-rich phase, where Si tetrahedra becomes coordinated with Al tetrahedra to form structures like Q^4(4Al) [43]. This preference for cross-linking Al atoms over Si atoms predominates at this moment. As the curing time increases, the structure would change from Al-rich N-A-S-H with Si/Al ratio of around 1 to Si-rich N-A-S-H with a roughly doubled Si/Al ratio [62, 63]. The generation of Si-rich N-A-S-H gels is triggered by the condensation reactions between Si-OH groups, stabilising the nanostructure with high cross-linking of Q^4(3Al) and Q^4(2Al) sites. **Fig. 3(b)** displays the N-A-S-H models (Si/Al ratio ≈ 1.5) with rising degree of disorder from crystalline to defective and amorphous structures [64]. Regarding the internal bond angle of O-Si-O, the tetrahedra in N-A-S-H gels shows limited distortion compared to the crystalline structure [65]. The external bond angle of T-O-T can vary between 120° and 180° in polymerised SiO_2 and AlO_2 [64, 66, 67].

The gel development can be described by the change in degree of reaction over curing time. Consequently, the volumetric model for alkaline activation can be built to track the change of volume fractions of solid gel particles. **Fig. 4(a)** demonstrates the volume changes of solid gel particles in AAF and AAMK [34]. Compared with AAF, AAMK exhibits a faster reaction, leading to a more rapid formation of solid gel particles by approximately 32.3%, while it contains a 26.6% higher open porosity based on the proposed model [34, 68]. The N-A-S-H gel matrix and gel pores will be further discussed at the next level in the following section.

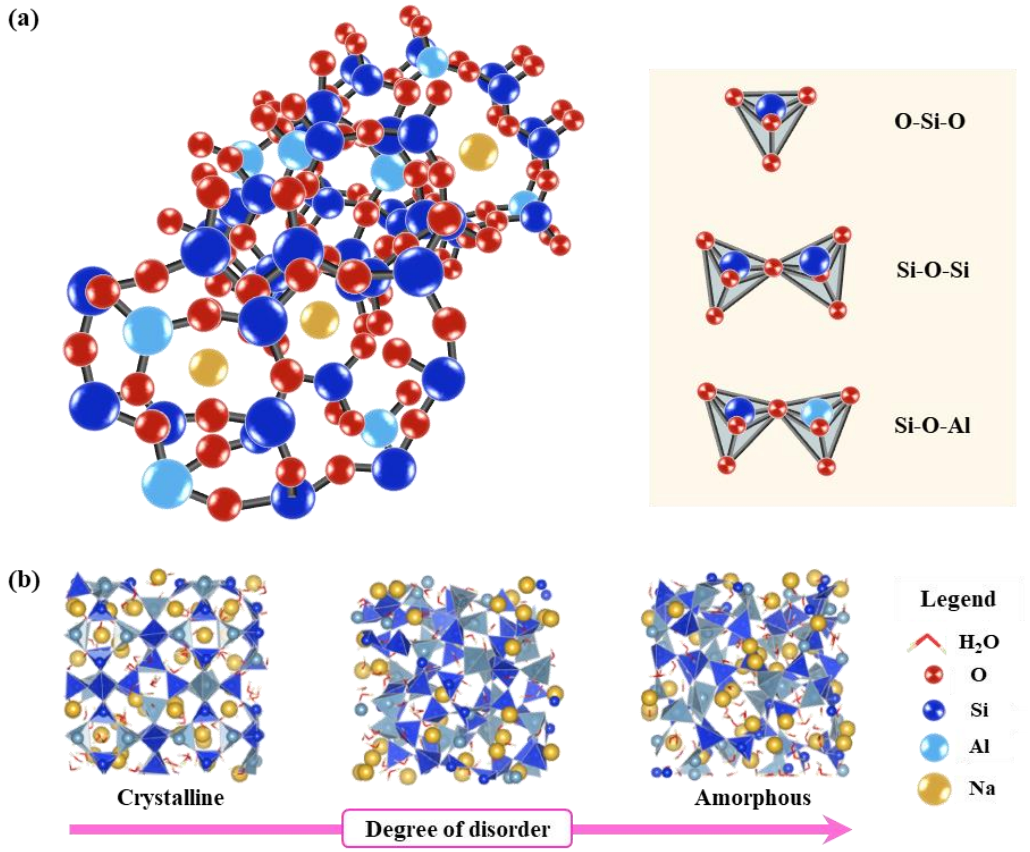

Fig. 3. Nanostructure of N-A-S-H regarding (a) 3D view, and (b) simulation from crystalline to amorphous N-A-S-H with Si/Al ≈ 1.5 (Adapted from Refs. [64, 69]).

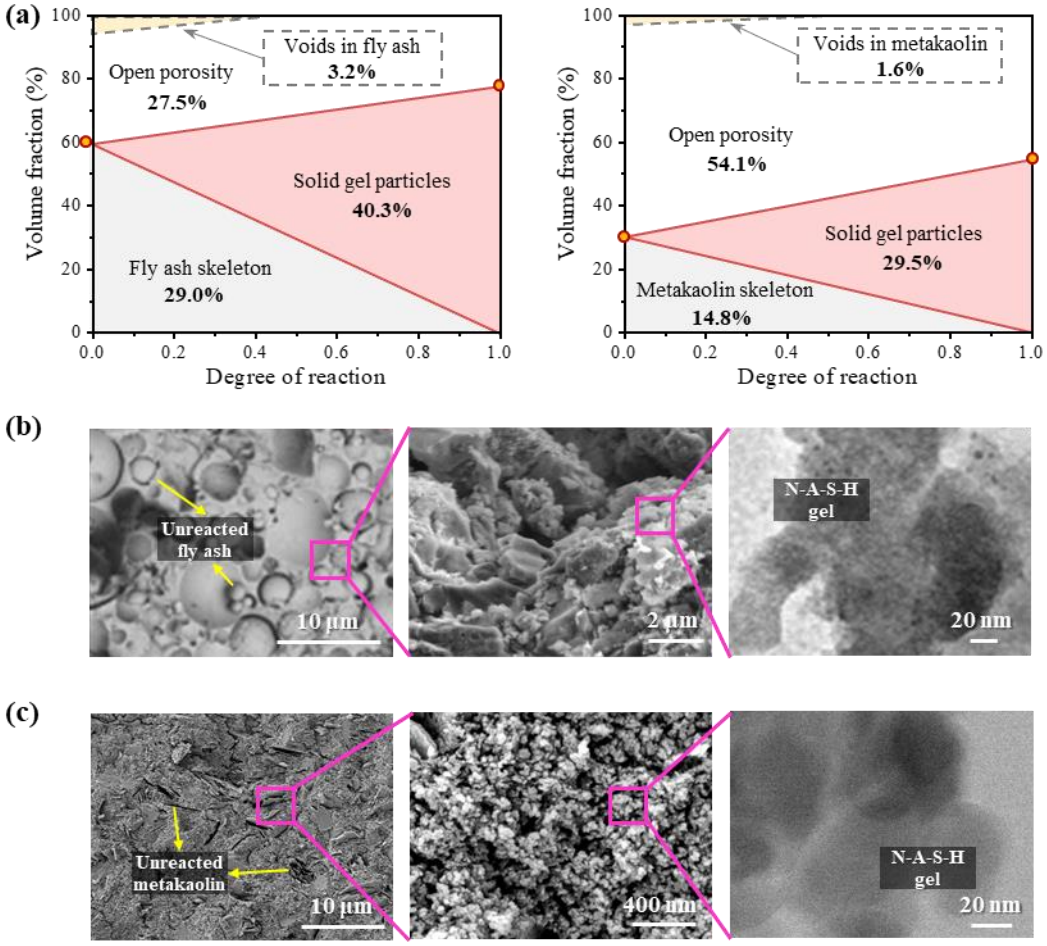

Fig. 4. Comparison of nanostructures in terms of (a) volumetric model of alkaline activation in AAF and AAMK [34], (b) SEM and TEM images of N-A-S-H gels in AAF [70-73], and (c) SEM and TEM images of N-A-S-H gels in AAMK [74].

3.1.2. Micromechanical properties

For the solid gel particles at nanoscale, it is very challenging to directly characterise the mechanical properties [44, 75]. Herein, the investigation has primarily relied on simulation studies. It was found that the level of structural disorder can significantly influence the mechanical properties of solid gel particles, as illustrated in **Fig. 3(b)**. Crystalline structure (order structure) is generally considered to exhibit better mechanical performance compared to amorphous structure (disorder structure) [64, 76].

As a sol-gel system, N-A-S-H contains solid particles dispersed in a liquid, which is heterogeneous with local aggregation into clusters [68]. With the increasing appearance of solid particles, the connections among clusters would lead to a percolation threshold indicated by a noticeable change of properties [34]. N-A-S-H has the nature of a true gel, referring to inconsistent gel porosity, excessive shrinkage, and strong sample disintegration (under sealed conditions) [77, 78]. Thus, the micromechanical responses have been suggested to be obtained at the level of solid gel particles downscaling from the gel matrix at Level 1 [34]. Using the Mori-Tanaka method, the elastic modulus of solid gel particles in AAF and AAMK was determined as 48.2 and 25.5 GPa, respectively [34]. This implies the possible difference among the existence of solid gel particles in different single precursor systems. The gel synthesised from AAMK was revealed to be richer in solid gel particles and twice as compliant as those found in the gel derived from AAF, while slightly different chemical compositions were also noticed in the previous experimental studies [34, 79, 80].

3.2. C-A-S-H solid gel particle

3.2.1. Nanostructure

The nanostructure of C-A-S-H has been described by analogy according to the structure of aluminium-containing minerals resembling disordered tobermorite-like [81-85]. This structure is formed of silicate chains inter-linked by layers of CaO. **Fig. 5(a)** introduces the nanostructure of C-A-S-H, which contains CaO layers, interlayer region and a so-called dreierketten arrangement with SiO_4 tetrahedra chains. The schematic illustration of Q^n in an interconnected silica structure is given in **Fig. 5(b)**. In the interlayer region, both alkali cations (Ca^+ and Na^+) and chemically-bonded H_2O are enclosed within the gel structure [43]. Here, alkali cations play a crucial role in neutralising the overall negative charge deduced by the substitution of Si^{4+} by Al^{3+} within the tetrahedral chain sites. Additionally, the nanostructure of C-A-S-H can be highly dependent on the Ca/Si ratio [81]. For low Ca/Si ratios, aluminium substitutions are prone to be tetrahedrally coordinated by silica sites, owing to tetrahedral replacement in the silica chains of C-S-H gel [86, 87]. Whereas, high Ca/Si ratios can result in random distribution of aluminium due to the substitution in the interlayer region, on the

particle surfaces or other reaction products [81, 88, 89]. Aluminium substitutions would therefore occur in octahedrally coordinated sites alongside hints of pentahedral coordination (with a ratio of octahedral/pentahedral coordination of around 3.5) [90, 91].

Different substitution positions of aluminium atoms have been proposed in C-A-S-H system, including bridging, pairing and ending sites, as depicted in **Fig. 5(c)**. In the context of chemical stability, the substitution of Si^{4+} by Al^{3+} significantly reduces the Gibbs free energy, leaving around 8 eV difference from the embedding energy of Si^{4+} [81]. Hence, there is a pronounced preference for aluminium occupancy in the bridging sites, attributing to energy disparities between distinct polymorphs and thermal energy [81, 92, 93]. The incorporation of Al^{3+} into the bridging SiO_4 tetrahedra leads to alterations in the Si-Al skeleton and the interlayer H_2O within the C-A-S-H gel [44]. This process enhances the crystalline arrangement and cross-linking degree by transitioning the layered C-S-H structure into a cross-linked C-A-S-H structure [43, 76, 94, 95].

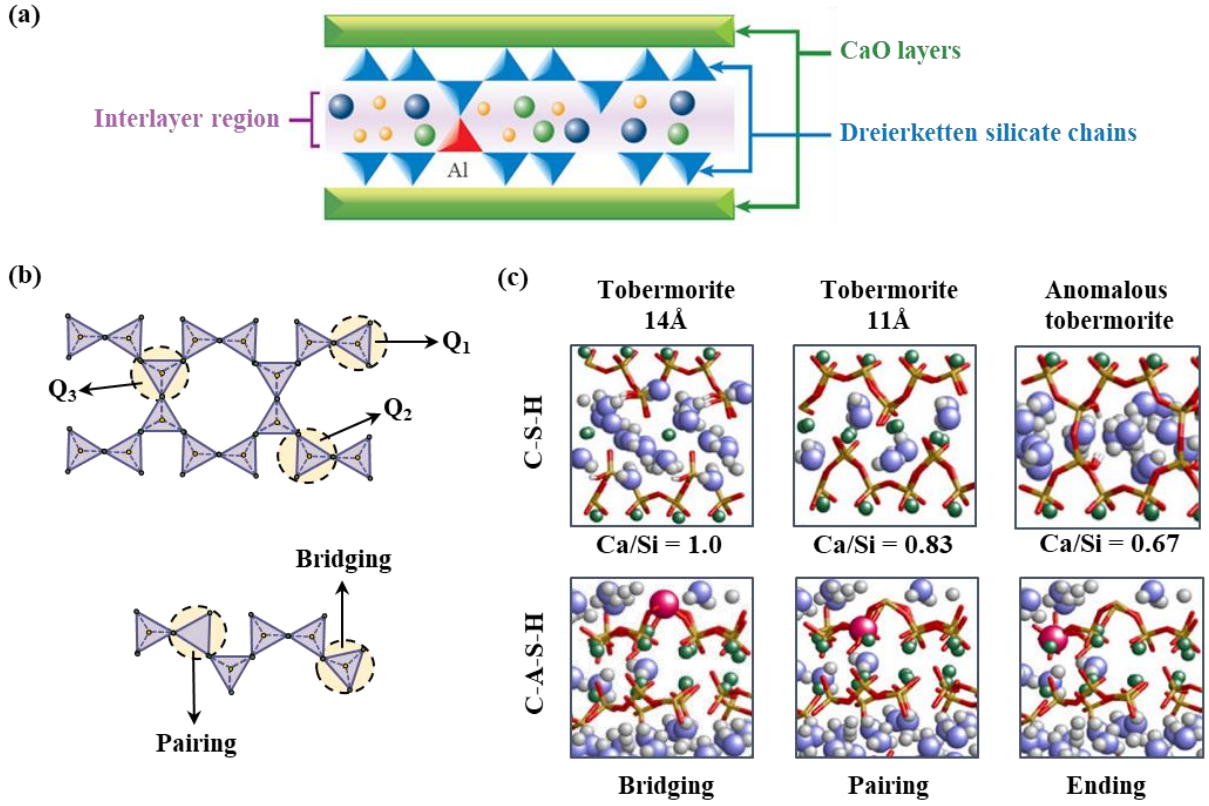

Fig. 5. Nanostructure of C-A-S-H: (a) overall tobermorite-like structure, (b) schematic illustration of Q^n in a silica chain and possible substitution positions for aluminium atom, and (c) structure of tobermorites in C-S-H and C-A-S-H with aluminium atom in the bridging, pairing and ending sites of a silica chain. (Adapted from Refs. [2, 81])

3.2.2. Micromechanical properties

Micromechanical properties of C-A-S-H can be associated with the nanostructure in terms of degree of cross-linking and chemical compositions. The increase of cross-linking level tends to enhance its mechanical responses [43, 76]. Specifically, the increase of Al/Si ratio in C-A-S-H solid gel has been

suggested to enhance its crystalline order and cross-linking degree, and therefore the mechanical responses [43]. The inclusion of Al branch structures serves to impede tensile loading and strengthen the soft interlayer region within the C-A-S-H solid gel [43, 44]. This, in turn, augments both the interlayer cohesive strength and stiffness [76, 94]. On the other hand, the alumino-silicate tetrahedral chains were reported to be less stiff than plain silica chains, suggesting the possibility of weakening the mechanical performance by increasing the Al content [81]. The overall mechanical properties can be determined by a combination of different factors, such as geometrical transformation, structure changes, Ca/Si ratio and charge neutraliser (Ca^{2+} or Na^{+}).

In terms of the aforementioned Al substitution positions, the mechanical properties of atomistic models with respect to tobermorite 14Å, tobermorite 11Å and anomalous tobermorite (**Fig. 5(c)**) were calculated. When the Al substitutions are located in silica chain pairing sites, the elastic modulus of solid gel ranges from 67.8 to 109.6 GPa. The elastic modulus of all models varies between 49.8 and 109.6 GPa at the bridging position. The anomalous tobermorite model exhibits the highest mechanical properties compared with others [81]. This reveals a noticeable dependence of mechanical performance on the configuration of aluminium atoms in C-A-S-H. Moreover, with the occurrence of calcium-aluminium replacement and decrease of Ca/(Al+Si) ratio, the main chain length seems to increase (more Q^2, Q^3, Q^4 and less Q^0 and Q^1 sites), thereby leading to the growth of elastic modulus [40, 81, 96, 97]. This implies that potential cross-links between layers, specifically Q^3 sites leading to the formation of a 3D nanostructure, which might positively affect the loading path between adjacent layers [81].

3.3. N-C-A-S-H solid gel particle

3.3.1. Nanostructure

With the incorporation of fly ash and slag, their different dissolutions and reaction mechanisms can trigger the interactions between different precursors in blend precursor system [46]. Especially, free Ca^{2+} can modify N-A-S-H gels during the reaction process by partially replacing Na^{+}, attributing to the strong polarising power of the aqueous Ca^{2+} relative to Na^{+} [43, 46, 52]. This results in the formation of N-C-A-S-H gel, as illustrated in **Fig. 6(a)**. Owing to the strong binding of Ca within the structure of C-A-S-H, the influence of Na+ on the formation of N-C-A-S-H is relatively insignificant [52]. It may be difficult to distort Ca^{2+} by the presence of Na^{+} due to the difference in polarising power between the two [98, 99].

Following this rearrangement process, the N-C-A-S-H gel exhibits mineral characteristics that bridge the gap between N-A-S-H and C-A-S-H gels. This means that it can maintain the inherent 3D aluminosilicate framework structure while tending to possess a composition more akin to that of C-A-S-H gel. However, the reorganisation and formation of N-C-A-S-H can strongly depend on different factors such as calcium content and pH conditions within the gel structure. **Fig. 6(c)**

demonstrates the transmission electron microscope (TEM) images of the gel morphologies under high-, medium-, and low-calcium environments. With high calcium content (CaO/SiO_2=3.2; SiO_2/Al_2O_3=2), a more lime-rich cluster can be observed, which indicates a combination of crystalline and amorphous phases. Under the medium-calcium condition (CaO/SiO_2=1.7; SiO_2/Al_2O_3=3.8), the morphology of the gel is characterised by foil-like shapes with the appearance of single grains [100]. As for the low-calcium environment (CaO/SiO_2=0.24; SiO_2/Al_2O_3=3), N-C-A-S-H gel can be identified with more globular-like morphology and relatively smaller angularity compared to C-A-S-H gel [25, 52].

In terms of pH conditions, a pseudo phase diagram has been reported to illustrate the stability and compatibility of N-A-S-H gel structure in terms of pH values, as displayed in **Fig. 6(b)**. The critical pH value of 12 is corresponding to the transition point between C-A-S-H and N-C-A-S-H pH measurements [52, 101]. When the pH condition is below 12, N-A-S-H would be either stable or accepting the ion exchange by Ca to form N-C-A-S-H. A full exchange might also appear to form C-A-S-H, whereas the gel would be remained in a 3D aluminosilicate structure instead of 2D [102]. When the pH value is around 12, the gel would degrade to C-A-S-H with the presence of free Ca [52].

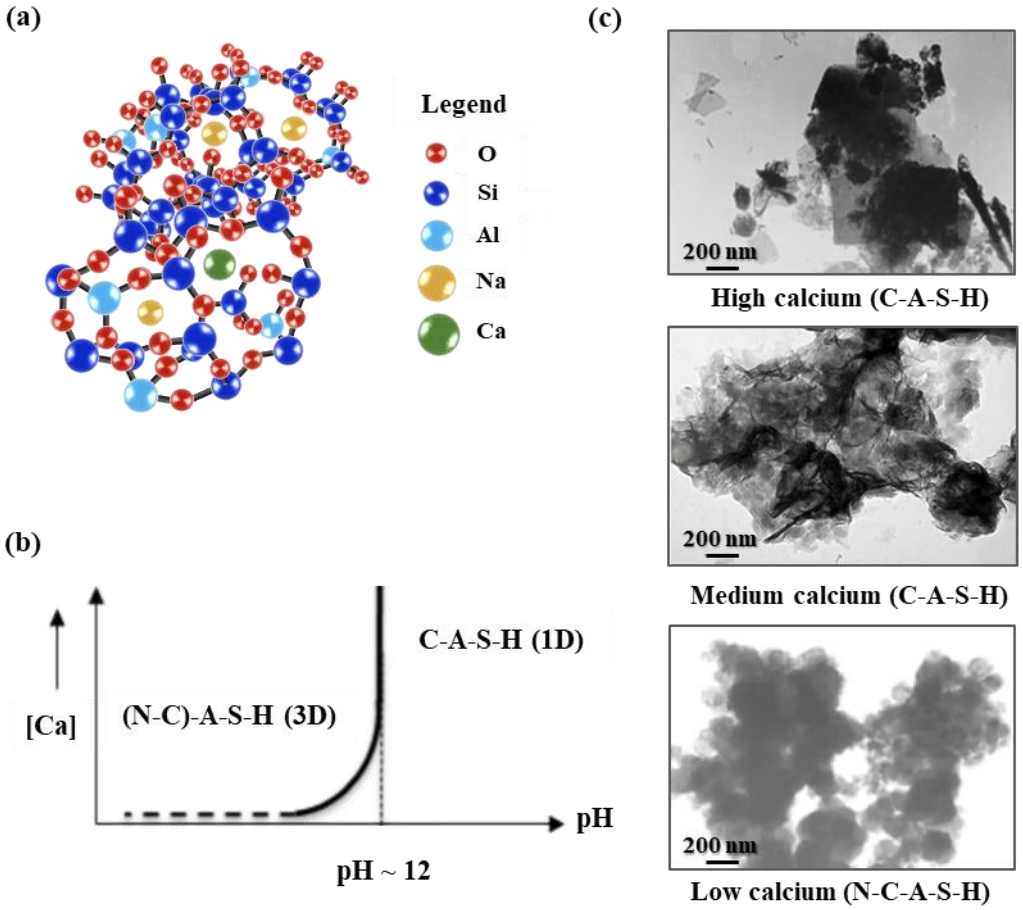

Fig. 6. Nanostructure of N-C-A-S-H: (a) overall 3D structure, (b) schematic illustration of the stability and degradation of N-A-S-H with pH, and (c) morphology of C-A-S-H and N-C-A-S-H gels under different calcium conditions detected using TEM [52, 100].

3.3.2. Micromechanical properties

The N-C-A-S-H can promote the enhancement of spatial heterogeneity of composition within the microstructure [53]. In the blend precursor system, the formation kinetics of N-C-A-S-H have been increasingly investigated, while the micromechanical properties are barely studied especially on the scale of solid gel particles. A few studies attempted to conduct qualitative and quantitatively analysis on the micromechanical responses of N-C-A-S-H gels based on nanoindentation tests [25, 103]. It was reported that the elastic modulus of N-C-A-S-H (around 15-23 GPa) fell between that of N-A-S-H and C-A-S-H, being higher than the former (4-20 GPa) and lower than the latter (up to 70 GPa) [25, 35, 37, 38]. The mechanical performance of N-C-A-S-H can possibly be corresponding to the aforementioned reorganisation in N-A-S-H by free Ca^{2+} to form N-C-A-S-H, leading to a retained N-A-S-H-like aluminosilicate framework and similar composition with C-A-S-H [25, 52]. To explore the micromechanical properties of N-C-A-S-H and thoroughly understand the structure-property relationship of such hybrid gels, molecular dynamics simulations can be employed to reveal the link between nanostructure and micromechanical features of N-C-A-S-H solid gel particles [104, 105].

4. Level I: Gel matrix

At Level I, the gel matrix is agglomerated by the solid gel particles and gel pores. The agglomeration process of N-A-S-H and C-A-S-H solid gel particles is commonly described by simplifying agglomeration model of C-S-H gel particles, which is recognised as the colloidal model [43, 100, 106, 107]. The tobermorite-like solid phases mentioned at Level 0 are assumed as the fundamental units, which are also identified as the basic building blocks [43]. The globules are then formed by packing of these blocks [102]. After further clustering of the globules, gel matrix is formed, as illustrated in **Fig. 7**. Herein, the inherent properties of 'globules' (i.e. solid gel particles) and gel pores (associated with the packing density of 'globules') will be discussed in depth based on the characterisation of nanostructure and micromechanical properties of different gel matrix.

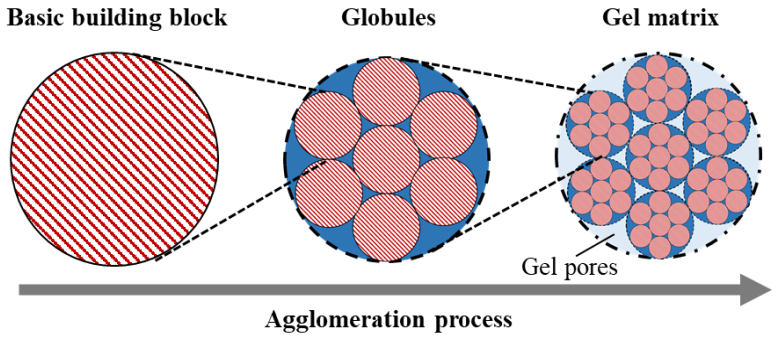

Fig. 7. Agglomeration of gel matrix [106].

4.1. N-A-S-H gel matrix

4.1.1. Nanostructure

The N-A-S-H gel matrix consists of primary globular polymeric entities with diameters of 0.8-2.0 nm, which are packed in a dense structure based on hydrolysis-polycondensation process [107-109]. A 3D network of aluminosilicates can be formed during the process, comprising Si-O-Si and Si-O-Al bonds in a highly cross-linked structure [109-112]. These bond formations coincide with the release of water into larger pores, facilitating the agglomeration of monomeric species into polymeric clusters, which subsequently develop into particles and consequently form gels [43]. It was mentioned that N-A-S-H gels are contingent upon the degree of reversibility [4]. When the polycondensation process approaches near irreversibility, it results in the formation of a space-filling gel, which eventually undergoes interconnection to create a continuous gel structure [68]. If the polycondensation rate exceeds the rate of bond breaking, the gels can develop with the inclusion of new monomers [113]. As such, reorganisation takes place in the N-A-S-H gel, which can restructure the gel into a more stable state. The morphology of the gel can be observed in **Fig. 4(b)** and **(c)**.

The nature of N-A-S-H gel nanostructure can be dependent on different factors, including curing time, temperature, and alkaline activator type [62, 102, 114, 115]. **Fig. 8** demonstrates the change of N-A-S-H gel nanostructure based on various curing conditions and activators. In general, longer curing time can benefit the formation of silica-rich products, favouring the strength development in geopolymer matrix. At the curing time of 3 h in **Fig. 8(a)**, the peaks ranging from around -92.1 to -112.3 ppm correspond to the presence of Q^4(nAl) sites, which are recognised as the N-A-S-H gels with a 3D structure containing Si in a variety of environments [102]. The dominance of Q^4 sites at 3 h indicates the formation of various Si-O-Al connections in aluminosilicate prepolymer structures, which can be attributed to the dissolution of active aluminate ions together with silicate heel ions [116]. With the increase of curing time, the spectral peak of ^{29}Si nuclear magnetic resonance (NMR) tends to shift positively with a focus on Q^4 sites. The presence of Q^1 and Q^2 at approximately -78 and -83 ppm can be ascribed to the gradual replacement of Si-O by Al-O during the polycondensation when increasing the curing time [98, 116]. As the reaction progresses to 24 h, the N-A-S-H gel becomes Si-richer, in which the determined volume fractions of Q^4(4Al), Q^4(3Al), Q^4(2Al) and Q^4(1Al) are 14.3%, 18.3%, 18.9% and 13.9%, respectively (**Fig. 8(b)**). This indicates that the extension of curing time can lead to the dissolution of active silicate and give rise to the silicate content, which promotes the strength development in matrix [116-118].

Fig. 8(c) shows the ^{29}Si NMR patterns of AAF cured at 40, 60 and 80 °C. When the curing temperature increases from 40 to 80 °C, there is a shift of the major spectral peak associated with Q^4(3Al) from -92.1 to -91.4 ppm. The heat curing was found to favour the dissociation of the -O-Si-O- and -O-Si-O-Al-O- bonds in fly ash and thus promote the pozzolanic reaction [116]. The presence

of peaks at around -103 to -108 ppm was found after 80 °C curing. These peaks are corresponded to the Q^4(2Al) and Q^4(1Al) sites, which are identified as Si-rich N-A-S-H gels in comparison with the Q^4(3Al) site (Al-rich N-A-S-H gels) [25, 119]. This suggests the formation and transformation of short-chain N-A-S-H gels from Al-rich to Si-rich, triggered by the curing at elevated temperatures up to 80 °C [116].

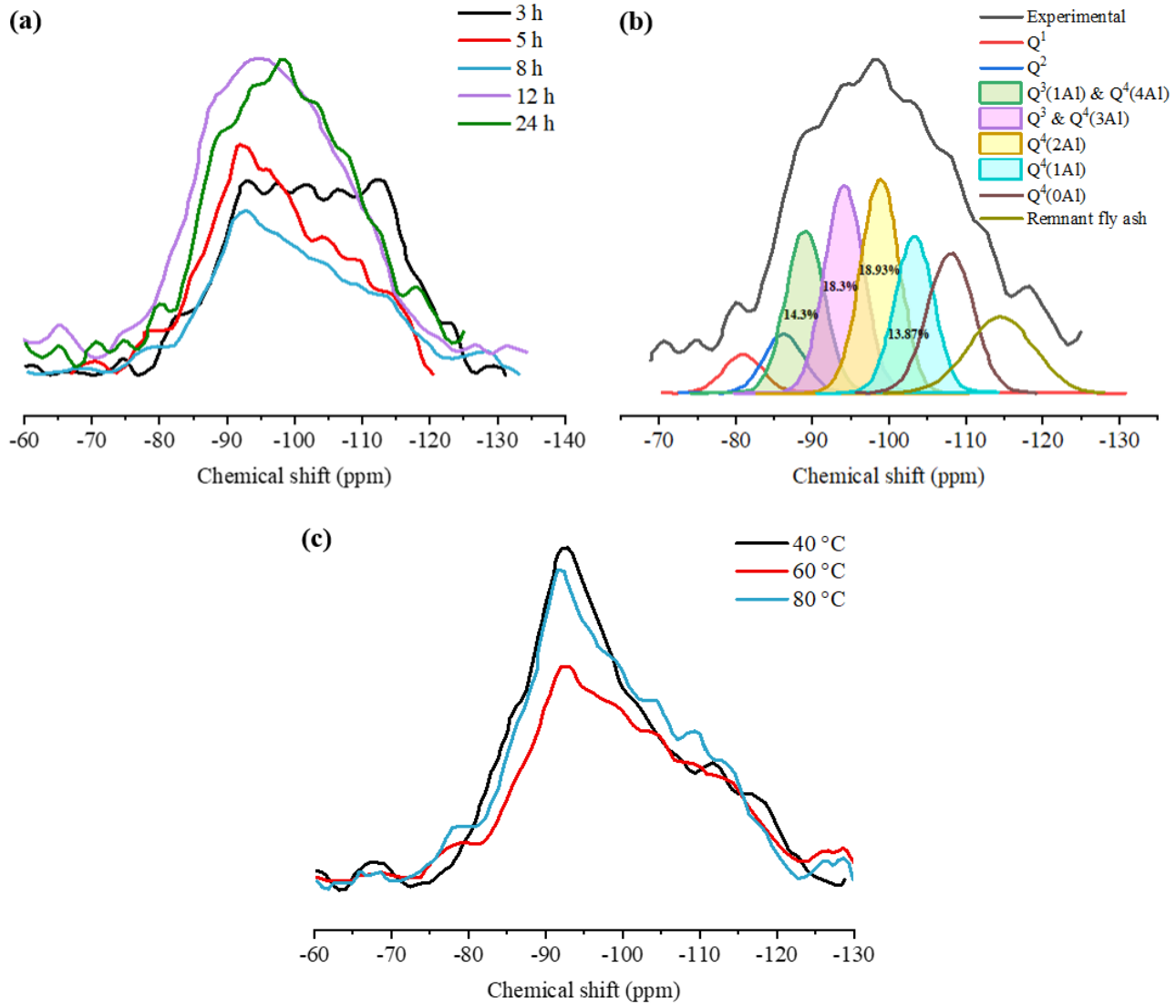

Fig. 8. ^{29}Si NMR spectra of AAF against (a) curing time with (b) the deconvolution, and (c) curing temperature [116, 120].

4.1.2. Micromechanical properties

To characterise the micromechanical features, different attempts have been made to explore the local elastic modulus and hardness of N-A-S-H gels in AAF and AAMK [121-128]. To identify the N-A-S-H phase from the nanoindentation results, statistical deconvolution can be performed, the first peak of which in the frequency distribution plot of elastic modulus corresponds to the N-A-S-H gel phase with the lowest elastic modulus [122]. The following peaks are associated with partially and unreacted precursors as these particles possess a higher elastic modulus compared to the gel phase [121]. After

the identification of N-A-S-H gel phase, the micromechanical properties of N-A-S-H gels can be determined, which are affected by different factors such as alkaline concentration and Si/Al ratio.

With the rise of Na_2O-to-fly ash weight ratio from 6% to 10%, the elastic modulus and hardness of N-A-S-H gels in AAF vary in the ranges of 12.7-15.5 GPa and 0.59-0.73 GPa, respectively [121]. A higher alkaline concentration can boost the activation of unreacted fly ash, leading to the enhancement of micromechanical properties in AAF. As for the Si/Al ratios, the elastic modulus of N-A-S-H gels tends to grow with the increase of Si/Al ratios, which is resulted from a greater density of binder gels induced by the rising Si content [123, 129]. Moreover, the Si-O bonds were found to exhibit a higher bond strength than Al-O bonds, indicating that a higher elastic modulus can be achieved in N-A-S-H gels if increasing the Si-O bonds with a higher Si/Al ratio [130]. On the other hand, to consider the micromechanical performance of pure N-A-S-H gels, it would be very challenging to separate them from other reaction products like the unevenly distributed crystal phase due to heterogeneity of AAC [121]. The future focuses can be attached to the development of other characterisation techniques to determine the micromechanical properties of pure N-A-S-H gels.

4.2. C-A-S-H gel matrix

4.2.1. Nanostructure

Compared with the C-S-H gel formed in PC pastes, the C-A-S-H gel was found to maintain a lower Ca/Si ratio of around 0.9 to 1.2 [102]. The nanostructure of C-A-S-H can be dependent on the Al/Si ratio within the gel. **Fig. 9** depicts the effect of incorporating aluminium on the structure of C-A-S-H based on the NMR results and TEM images. In the C-S-H gel, the ^{29}Si NMR pattern is deconvolved with respect to Q^1, Q^2_p and Q^2_b (**Fig. 9(a)**), which respectively refers to the terminal silicate tetrahedra and Q^2 with the pairing and bridging positions, as mentioned previously [131-133]. Obviously, Q^1 dominates the structure when Al/Si ratio is 0, which takes up 75.6% of the gel. With the increase of Al/Si ratio to form C-A-S-H gels, as shown in **Fig. 9(b)** and **(c)**, the deconvolution of them reveals the existence of Q^2_p(Al IV), corresponding to the pairing silicate tetrahedron with the bridging Al (IV) [134-136]. This can be ascribed to the incorporation of aluminium, which occupies bridging sites and transfer the initial Q^1 into new Q^2_p(Al IV) sites [88, 131]. As a result, the silicate chain can be elongated with the increased fraction of Q^2 by 33.4% and the reduction of Q^1 to down to 42.4% when the Al/Si ratio reaches 0.20 [131, 135]. Moreover, the rise of Al/Si ratio from 0.05 to 0.20 can result in the increasing amount of Q^2_p(Al IV) by 24.1%, implying that the aluminium is mainly occurred as IV-fold coordinated. Different structures in the alumino-silicate chains within C-A-S-H gels are illustrated in **Fig. 9(d)**.

Other than the IV-fold coordinated aluminium (Al(IV)), there are also V-fold (Al(V)) and VI-fold (Al(VI)) coordinated signals, which can be associated with the dissolved aluminium in C-A-S-H interlayers and the third aluminate hydrate (i.e., an Al-rich phase precipitated on the surface of C-A-

S-H gel), respectively [91, 133, 137]. The spatial impression of Al(IV), Al(V) and Al(VI) is schematically illustrated together with the ^{27}Al NMR spectra of C-A-S-H at Al/Si ratios of 0.05 and 0.20 shown in **Fig. 9(e)**. At both Al/Si ratios, the predominant peak represents Al(IV), which may be charge-balanced by Ca^{2+}(presented as $Al(IV)_{-a}$ in **Fig. 9(d)**) and Al(V) and/or Al(VI) (denoted as $Al(IV)_{-b}$) [138]. As for the nanomorphology, the gel transitions from grains and blade-like structures (within 1-2.5 h after the reaction) towards foil-like structures (over 24 h) [100, 139]. **Fig. 9(f)** presents the change of C-A-S-H gels with the increase of Si/Al ratio. A foil-like shape can be observed in all specimens, which tends to become darker, denser and more compact when rising Al/Si ratio [100, 131, 133, 140, 141]. This indicates that the substitution of Si by Al can potentially modify the charge distribution in globules and give rise to more significant attraction between them [100, 131].

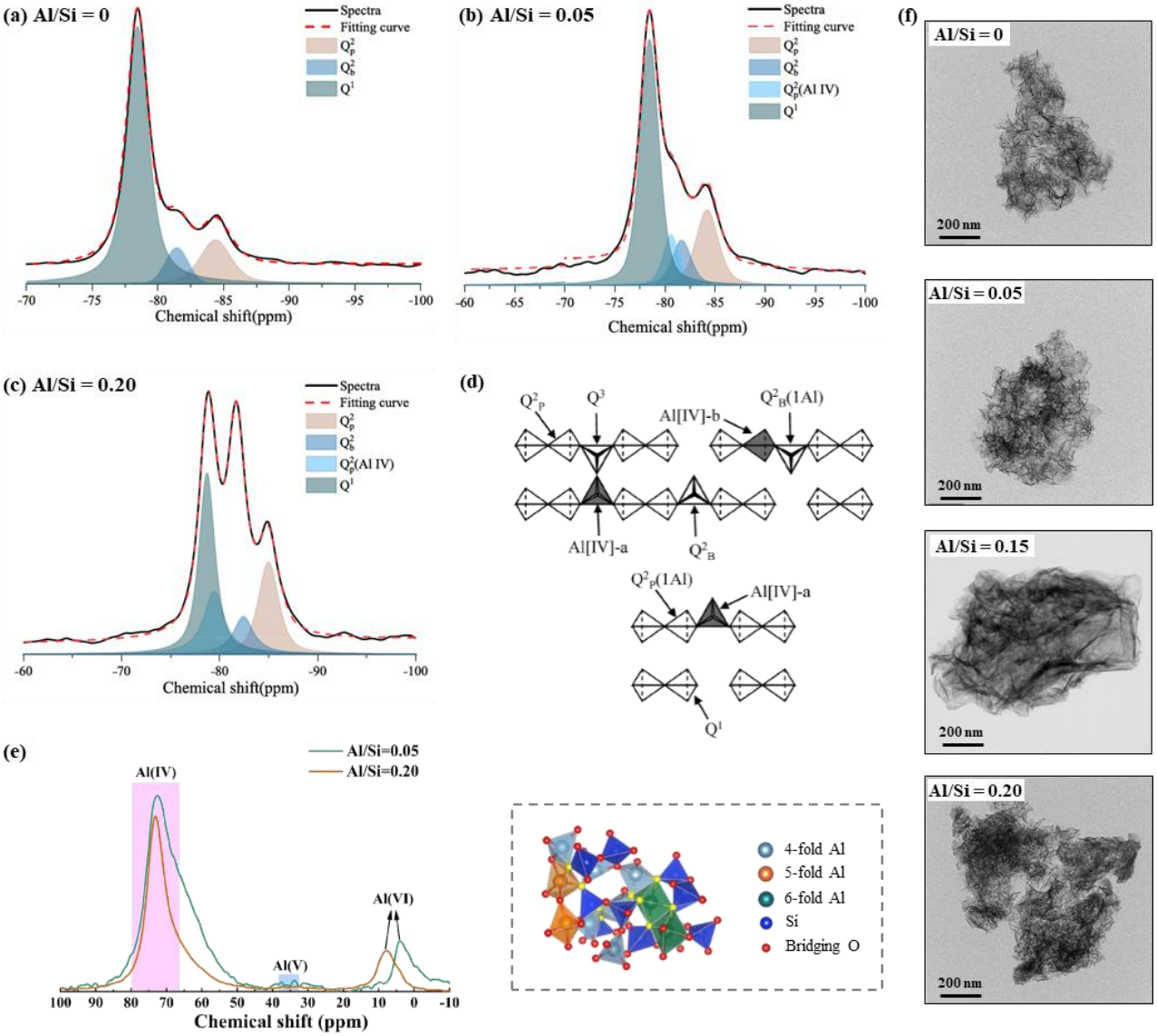

Fig. 9. ^{29}Si NMR spectra of (a) C-S-H and C-A-S-H with (b) Al/Si=0.05 and (c) Al/Si=0.20, with (d) Deconvolution based on alumino-silicate chains in C-A-S-H; (e) ^{27}Al NMR spectra of C-A-S-H with different Al/Si ratios and (f) Corresponding TEM images (Adapted from Refs. [131, 133, 138, 142]).

Two types of packing referring to low-density and high-density were proposed to describe C-A-S-H gels [40, 43, 106, 143]. The low-density packing configuration bears resemblance to the random close packing, while the high-density packing configuration aligns closely with the face-centred cubic lattice packing arrangement [43, 144]. The packing density of low-density and high-density C-A-S-H gels is in the ranges of 0.63-0.71 and 0.68-0.79, respectively. Thus, the porosity values of low-density and high-density C-A-S-H gels are characterised as 29-37% and 21-32%, respectively. Therefore, C-A-S-H gels exhibit diverse ranges of packing density, spanning from 0.63 to 0.79, and gel porosity ranging from 21% to 37% [40, 43]. These characteristics are influenced by the spatial availability for C-A-S-H gel packing, with denser packing approached to the precursor particles and looser packing in regions further from them [40, 145, 146]. As for the aforementioned nature of activator, the activator type can modify the structure of C-A-S-H gels. In particular, C-A-S-H gels with SH exhibit a comparatively higher gel porosity ranging from 21% to 37%, whereas those activated by SS demonstrate a lower value from 21% to 29% [40].

4.2.2. Micromechanical properties

Considering the micromechanical properties, it is summarised that the elastic modulus of individual phases in AAS follows an ascending order of pore < reaction products < unreacted slag [37, 147-150]. The reaction products in AAS can be divided into two different groups based on their micromechanical performance, including outer reaction product consisting of C-A-S-H gels and inner reaction product composed by the combination of C-A-S-H gels and layered double hydroxides [151-153]. With different types of alkaline activators, the volume fraction of C-A-S-H gels can be affected. The C-A-S-H gels were found to take up 68.0% and 47.3% of the reaction products when activated by SH and SS, respectively [151]. Since the microstructure features are generated faster in SH-activated slag (within a few hours) than SS-activated slag, the corresponding strength development tends to be slower in the later one [35, 154-156]. The alkaline concentration (molarity) and silica modulus were found to have limited influences on the elastic modulus of C-A-S-H gels [35]. It was reported that the elastic modulus of C-A-S-H gels and inner reaction product in AAS were stabilised at around 26 GPa and 35 GPa, respectively, no matter which activator was used [151, 157]. Thus, the micromechanical responses of C-A-S-H gels can be dependent on the distance to unreacted particles, degree of reaction and chemical compositions modified by alkaline activators.

4.3. N-C-A-S-H gel matrix

4.3.1. Nanostructure

As the formation of N-C-A-S-H gels follows the aforementioned process, the agglomeration of N-C-A-S-H gel particles should be similar to N-A-S-H [46, 52, 107]. However, the polarising effect of Ca^{2+} can induce the rearrangement of the aluminosilicate structure by distorting the Si-O-Al bonds, resulting in the formation of Si-O-Ca bonds [54]. This structural modification leads to less

polymerised structures in N-C-A-S-H gel matrix with a decreasing degree of cross-linking, which can finally result in a comparable structure to C-A-S-H gels [52]. **Fig. 10** presents the evolution of nanostructure in AAFS from 1 to 28 d. A negative shift of the broad peak from -84.2 to -85.7 ppm together with the change of the broad band centre from -107.2 to -105.9 ppm denotes the further polymerisation with a higher degree of cross-linking of gels over time [25]. As N-C-A-S-H gels are associated with Q^3(1Al) and Q^4(4Al) sites located at around -88 ppm, the increase of curing ages can lead to a higher composition of N-C-A-S-H gels from around 11.1% at 1 d to 14.6% at 28 d [46, 119].

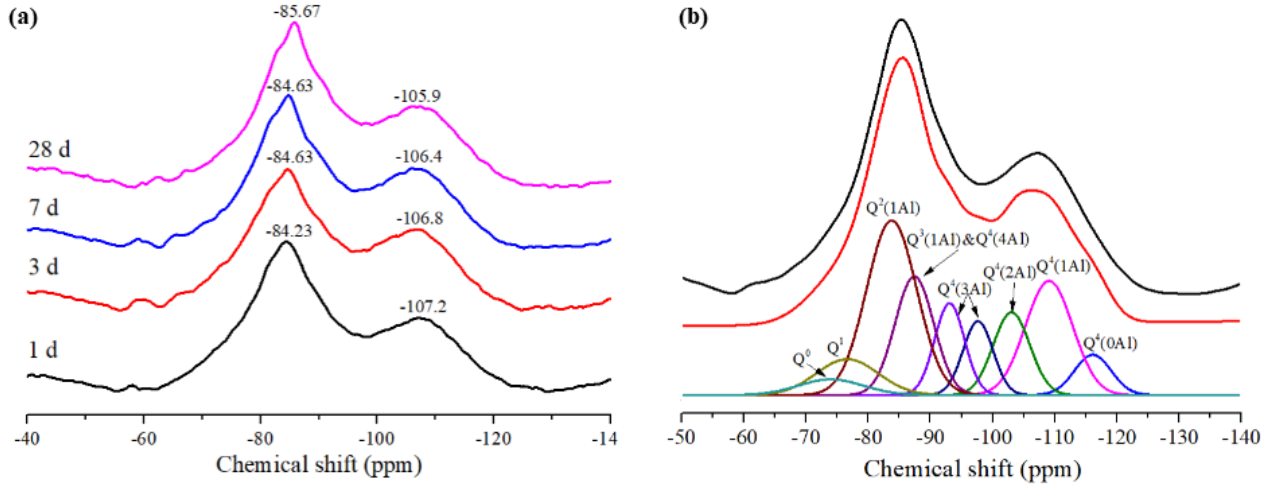

Fig. 10. (a) ^{29}Si NMR spectra of AAFS at different curing ages from 1 to 28 d with (b) the deconvolution results on 28 d [25].

4.3.2. Micromechanical properties

The micromechanical properties of N-C-A-S-H gels are mostly studied via nanoindentation tests on blended AAC with calcium-rich precursors like AAFS [43, 103]. In terms of the level of cross-linking, the order was proposed as: N-A-S-H < N-C-A-S-H < C-A-S-H gels [43]. Correspondingly, the elastic modulus of N-C-A-S-H gels tends to lie between that of N-A-S-H and C-A-S-H gels based on their different microstructural features. Comparing the N-(C)-A-S-H and C-(N)-A-S-H gels, the former exhibits the Si/Al ratio of around 6, whereas the later has a Si/Al ratio of around 3 [158]. Accordingly, the elastic moduli of N-(C)-A-S-H and C-(N)-A-S-H gels were detected, which were around 15.5 GPa and 17.8 GPa, respectively [158]. It was proposed that a relatively higher Si/Al ratio of up to 4.3 in the gel showed lower level of dissolution and thus lower elastic modulus compared to the gel with a lower Si/Al ratio at around 2.4 [158]. This indicates that the variation of elastic modulus in N-C-A-S-H gels is associated with the degree of dissolution from the precursors, which is significantly affected by the alkalinity of different alkaline activators [125, 158]. The elastic modulus of N-C-A-S-H gels was found to go up continuously from around 19.0 GPa to 22.7 GPa with the curing time from 1 to 28 d [43].

5. Level II: Paste

Level II refers to the paste level, which is composed of unreacted precursors, reaction products (i.e., gel matrix in Level I) and pores. At this level, the unreacted precursors including fly ash and slag are reviewed and discussed in terms of the dissolution and reaction mechanisms. The evolution of pore structures and reaction products is also summarised at paste level.

5.1. Unreacted particles

5.1.1. Microstructure

It is recognised that the reaction of precursor that leads to the formation of reaction products is essential to the determination of multiscale properties of AAC [46, 51, 159]. The morphology and chemical compositions of precursors such as fly ash and slag have been extensively investigated through SEM and EDS tests [53, 155, 160, 161]. The distribution and microstructural evolution of these particles can be heterogeneous and highly dependent on their particle sizes, precursor systems (single or blend system), activator types, curing ages and local alkaline environment [43, 111, 162-164]. Moreover, the microstructural evolution of unreacted particles was also in-situ monitored using non-destructive XCT, enabling the detection of internal 3D structure of AAC at microscale [165-167]. In particular, the reaction process of unreacted particles can be observed and reconstructed to characterise the consumption of unreacted particles and the formation of subsequent binder gels. **Fig. 11** demonstrates the particle dissolution and reaction of fly ash and slag particles in AAFS paste at different curing ages by XCT, along with the corresponding SEM and BSEM images. The time-dependent evolution of particle structure can be directly observed.

For both fly ash and slag particles, the reaction process includes the dissolution of particle and the development of surrounding matrix [163]. In the unreacted fly ash particle, the dissolution occurs with the rupture of Si-O-Si and Al-O-Al bonds, which exhibits inconsistent degree of reaction in different directions with an increase of irregularity from a spherical to more angular shape as time goes by. Due to the heterogeneity of fly ash particles, in which the distribution of inert crystal phases and reactive amorphous phases can be random, the parts that contains more amorphous phases are prone to react faster than the rest of particles [163, 168]. The formation and precipitation of reaction products are localised in the dissolved area of fly ash particles, which can be identified as inner and outer products based on the relative position to the initial particle boundary [43]. The initial formation of inner products has been found to physically impede the diffusion of ions, which can be difficult to penetrate from outside the particle into N-A-S-H gels as the reaction proceeds [107, 162, 163].

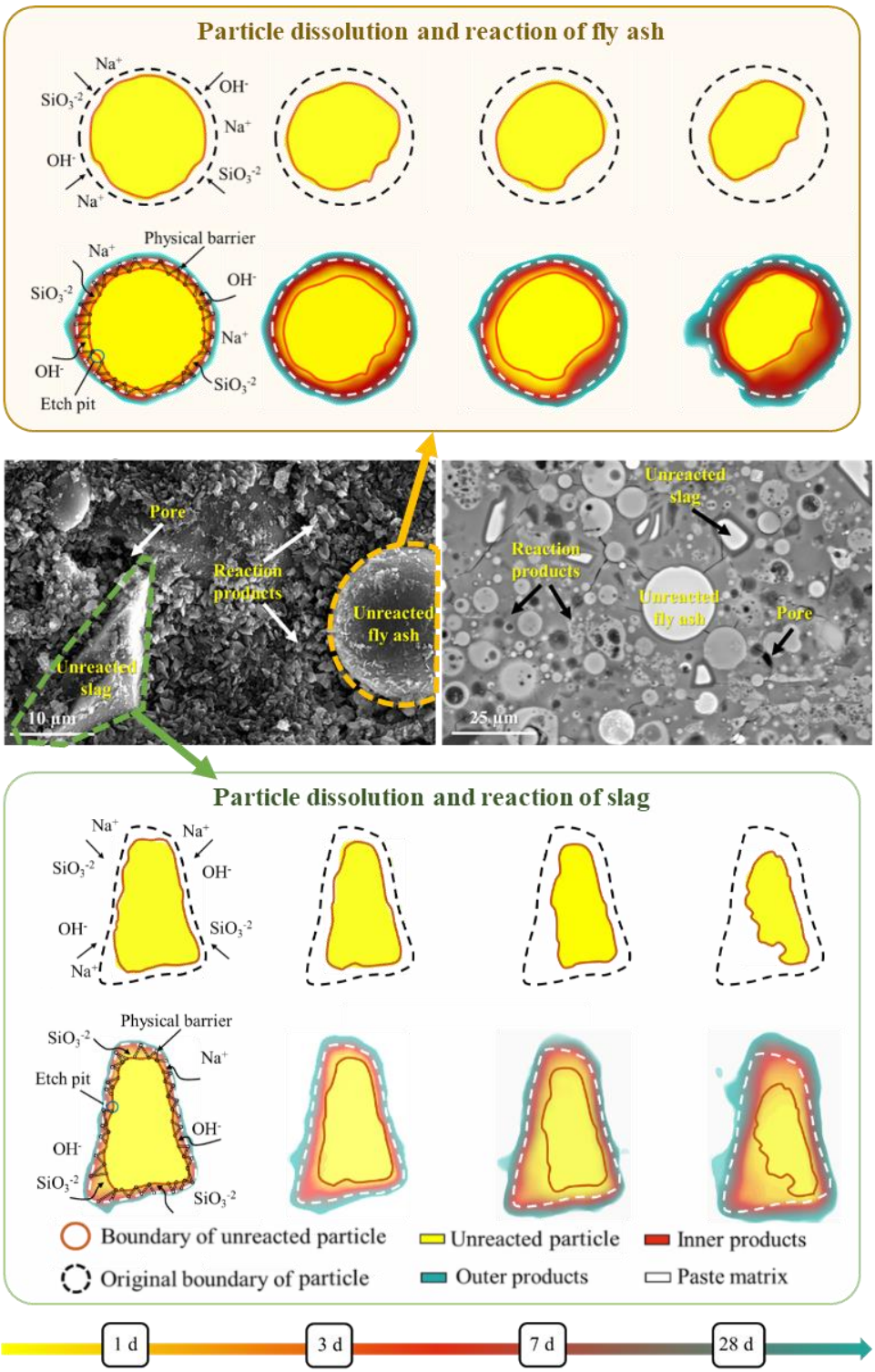

Fig. 11. Dissolution of fly ash and slag and formation of reaction products in AAFS (Adapted from Refs. [43, 163]).

As for the unreacted slag particle, it shows a less spherical shape compared to fly ash in **Fig. 11**. The dissolution of slag particles occurs by breaking the Ca-O and Si-O-Si bonds. Similar to fly ash, the dissolution of slag exhibits inhomogeneous characteristics with increasing irregularity of the remnant particle from 1 to 28 d. The formation of C-A-S-H gels can be further observed with the increase of curing ages, acting as a physical barrier that surrounds the remained core particles and thereby slows down the further reaction process when approaching 28 d [43, 169]. It is worth noting

that in a blend precursor system like AAFS, the interaction between fly ash and slag particles can also be crucial to the microstructure evolution, since different ions are dissolved from these particles (i.e., Si and Al from fly ash; Ca, Si and Al ions from slag) [53, 161, 163]. The interaction mechanisms between both particles were characterised in two stages: the early stage from 1 to 3 d and later stage from 7 to 28 d. No apparent interaction between fly ash and slag particles was detected during the early stage, whereas the diffusion of Ca^{2+} had a pronounced effect on accelerating the formation of C-A-S-H and N-A-S-H gels. It can also trigger the formation of hybrid gels as Si ions near fly ash particles would prefer the reaction with Ca^{2+} to form N-C-A-S-H gels [161, 163].

5.1.2. Micromechanical properties

The micromechanical properties of unreacted precursors in AAC have been experimentally explored via nanoindentation tests. In AAF paste, the elastic modulus of unreacted fly ash particles is dependent on their mineral features with an overall range from around 30 to 140 GPa [37-39]. Among different chemical compositions of fly ash, the Fe-rich ones achieve the highest elastic modulus, ranging from 71.0 to 137.7 GPa, whereas Ca-rich fly ash particles exist a relatively lower value, i.e., 75.7-91.2 GPa [39]. The elastic modulus of Si-rich fly ash is around 82.9 GPa, while the worst performance has been reported in Al-rich fly ash with an elastic modulus of 33.3-65.4 GPa [39]. As for AAS paste, the elastic modulus of unreacted slag is in the range of 46-70 GPa, with the hardness of approximately 6 GPa [35, 170]. In terms of blend AAFS paste, the combination of fly ash and slag as a whole unreacted particle phase is tested with an overall elastic modulus of more than 65 GPa [43, 170]. Whereas, the individual particles are analysed in AAFS with an elastic modulus of around 71.6 and 48.5 GPa in fly ash and slag, respectively [43]. As the curing time increases from 1 to 7 d, the elastic modulus of fly ash exhibits a reduction by up to 9.56%, while that of slag is stabilised at around 49 GPa. This can be attributed to the discrepancy between dissolution and reaction mechanisms of both types of precursors as mentioned previously.

5.2. Reaction products

5.2.1. Microstructure

The microstructure of reaction products in AAC can be affected by different factors such as activator type, curing time and slag content, which are generally characterised using SEM and EDS techniques. The chemical compositions of reactions products can be analysed using the ternary CaO-SiO_2-Al_2O_3 and SiO_2-Al_2O_3-Na_2O diagrams. **Fig. 12** illustrates the effect of slag content and alkaline activator on the chemical compositions of reaction products. The mixture of reaction products including C-A-S-H, N-A-S-H and N-C-A-S-H gels with other minor phases can be detected. For N-A-S-H gels, the Al/Si ratio of Si-rich N-A-S-H gels is close to 0.5, whereas Al-rich N-A-S-H gels may approach an Al/Si ratio of more than 2 depending on the compositions [171]. The N-A-S-H-rich region is commonly identified with the Al/Si ratio ranging from 0.08 to 0.5 and Ca/Si ratio of 0-0.3 [52, 53].

In terms of C-A-S-H gels, they are characterised at the region with the Ca/Si ratio varying roughly between 0.67 and 3, as shown in **Fig. 12(a)**. Additionally, the hybrid N-C-A-S-H gel was segmented into two different types, which includes low-calcium substituted N-(C)-A-S-H gel from the reaction of fly ash and C-(N)-A-S-H gel with low sodium content formed by the activation of slag [171]. The Ca/Si ratio of N-(C)-A-S-H gels was reported to locate within the range of around 0.14-0.33, while C-(N)-A-S-H gels tend to have a higher Ca/Si ratio of approximately 0.45-10 [46, 52, 99, 172, 173].

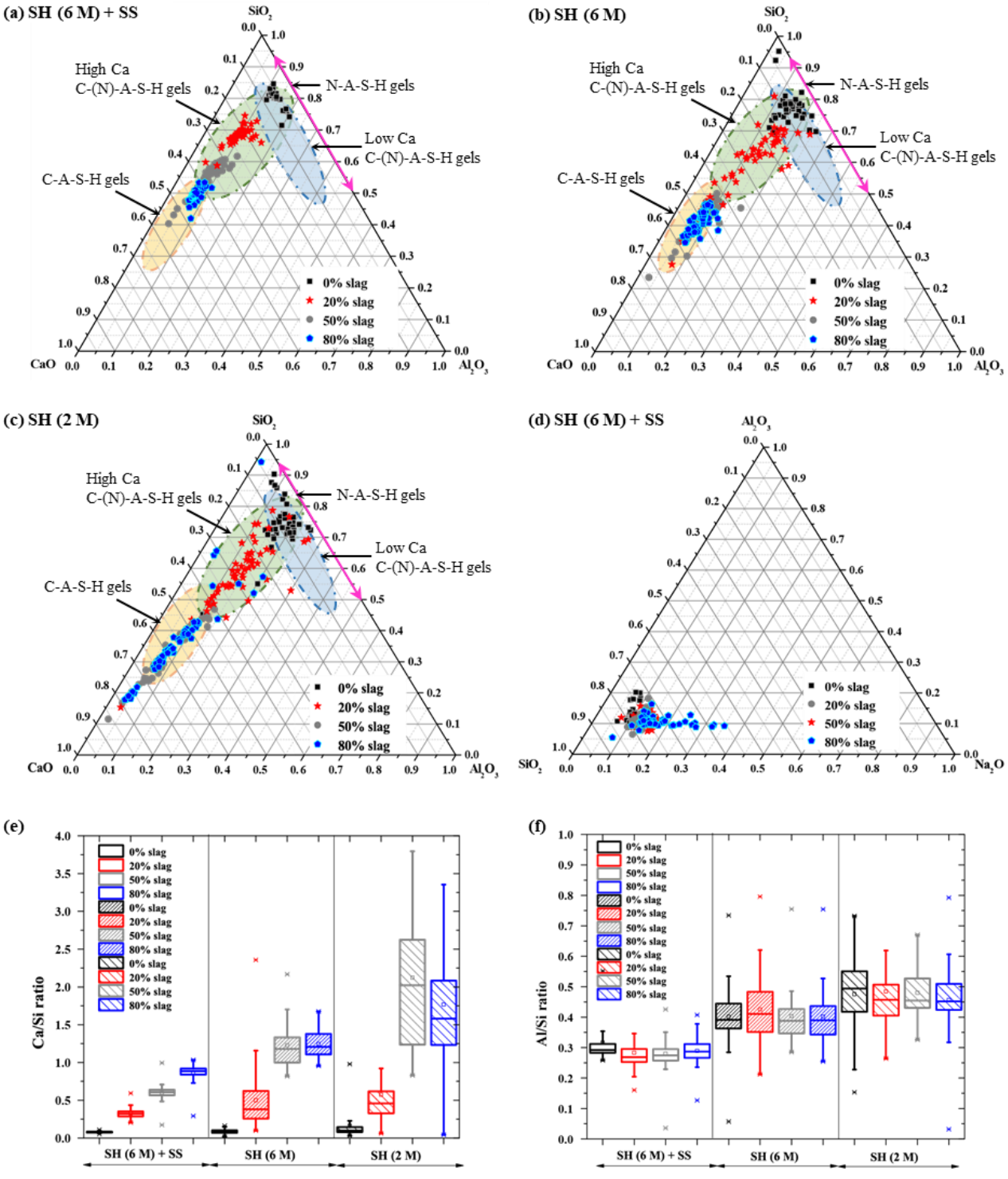

Fig. 12. Composition ternary diagram in (a-c) CaO-SiO_2-Al_2O_3 and (d) SiO_2-Al_2O_3- Na_2O for AAFS with various slag contents and alkaline activators, accompanied by the statistical distribution of (e) Ca/Si and (f) Al/Si ratios based on the EDS analysis (Adapted from Refs. [43, 52, 53, 103, 174].

Fig. 12(b-d) presents the influence of alkaline activators on the compositional changes within the paste [53]. Compared with AAFS activated by the combination of sodium hydroxide and sodium silicate, the specimens activated by sodium hydroxide exhibit relatively higher Ca/Si and Al/Si ratios with more inhomogeneous chemical distribution. This implies that increasing amount SiO_2 may depress the precipitation of zeolite crystal and preferentially trigger the formation of N-C-A-S-H instead of C-A-S-H [46, 53]. The statistical distribution of Ca/Si and Al/Si ratios based on the EDS results is shown in **Fig. 12(e-f)**, indicating a more pronounced effect of slag content on the chemical compositions of binder gels in AAFS in comparison with the activators [53]. With the incorporation of slag from 0 to 80%, the chemical composition of reaction products moves from low-calcium towards high-calcium region, inferring the change of binder gel contribution from N-A-S-H-rich to C-A-S-H-rich in the blend precursor system. As per the findings on different binder gel matrix at Level I, the phase transformation at paste level can be quantified in terms of change of volume fractions in binder gels.

Fig. 13 illustrates the microstructure and phase assemblage of reaction products and unreacted particles in AAFS characterised using NMR. From 1 to 28 d, C-A-S-H denotes a gel structure with more links in the chain, which takes up 34.9% of the paste at 28 d [25]. The volume fraction of N-C-A-S-H stabilises at around 14.6% after 28 d, suggesting an enhancement in the cross-linking of gel structure as the curing time increases. Furthermore, a higher degree of polymerisation can be found in N-A-S-H gels, occupying approximately 35.9% to 42.6% of AAFS paste at up to 28 d of curing [25]. The understanding of reaction products and identification of individual phases can provide microstructural basis for the characterisation of micromechanical properties and macroscopic performance of AAC.

On the other hand, the reaction products in AAC can be influenced by the mixing approaches. Given the caustic nature of alkaline activators, one-part AAC has been introduced, allowing for the pre-mixing of aluminosilicate binders and solid alkaline activators. Consequently, only water needs to be added to activate the mixture [175, 176]. For one-part AAC, the dissolution of both dry precursors and solid alkaline activators occurs simultaneously, resulting in a reaction process that includes four steps: pre-induction, induction, acceleration (i.e., formation of reaction products), and deceleration [175, 177, 178]. The duration of each step can be affected by the silica solubility of different alkaline activators. For instance, the sodium silicate particles exhibit a lower solubility than that of potassium silicate particles, due to the smaller hydration sphere of potassium ions [49, 175,

179]. Thus, the incorporation of potassium silicate powders in AAC can lead to a higher intensity of dissolution and a faster induction period compared to the other activator.

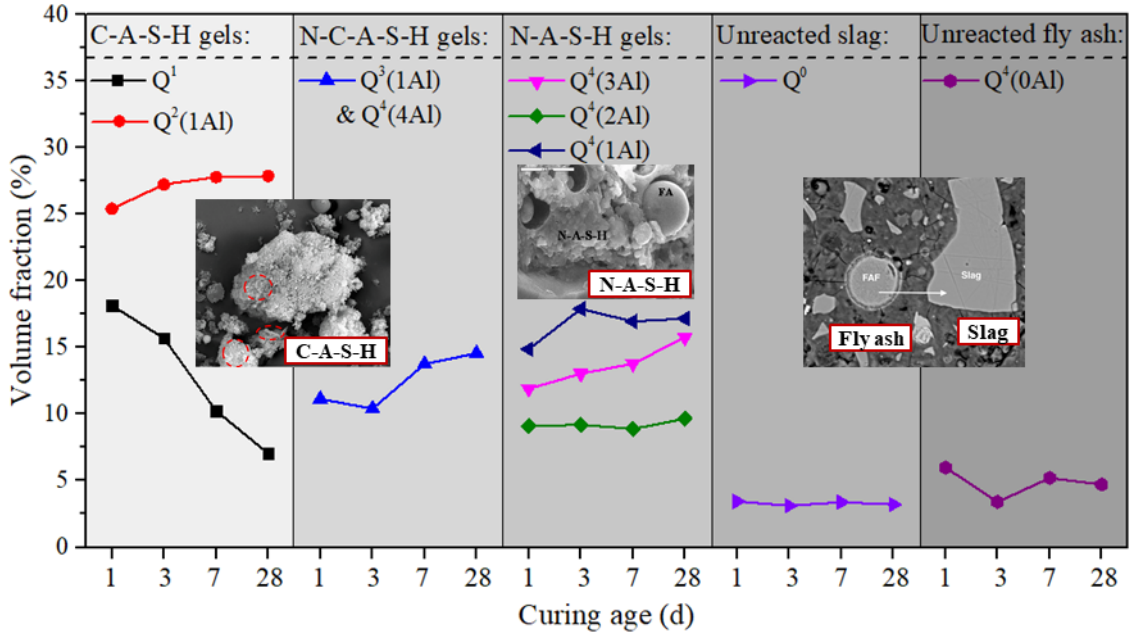

Fig. 13. Phase assemblage of AAFS paste at different curing ages [25, 53, 133, 180].

5.2.2. Micromechanical properties

In recent years, the micromechanical properties of reaction products are increasingly studied at paste level in different types of AAC. In AAF, the elastic modulus of N-A-S-H is dependent on the aforementioned curing conditions and choice of alkaline activators, which varies from 4 to 20 GPa [37-39, 43]. C-A-S-H in AAS tends to exhibit a higher elastic modulus than N-A-S-H, ranging from 12 to 47 GPa with the hardness of 0.3-2.5 GPa, which is strongly associated with the mix design [35, 40, 43]. For the N-C-A-S-H gel in AAFS, the elastic modulus was found to go up from 15.6 to 23.9 GPa as the curing time reaches 28 d [25]. This implies that the transformation among different reaction products can be crucial to the evolution of their micromechanical properties.

5.3 Pores

The multiscale pore structure of cementitious materials can be characterised in different ways. In PC concrete system, the pores are distinguished as gel pores (0.5-10 nm), capillary pores (10 nm-10 μm), and air voids (> 10 μm) [43, 181]. However, the pore size distribution in AAC can differ from that in PC system due to the discrepancy in chemical compositions and reaction kinetics. The pore structure in AAC can be categorised in three different types, corresponding to the length scale from Level 0 to Level II in this review [182]. Level 0 represents molecular pores (< 2 nm) existing in solid gel particle networks. Level I is associated with nano pores (2-100 nm) from gel interstices in gel matrix. Level II stands for micro and meso pores (100 nm-10 μm), which can be composed by a combination of cracks, hollow voids induced by partially reacted particles, defects and fillers in AAC paste [182].

Pores with a size of greater than 10 µm are referred to macro pores induced by air bubbles, which can be recognised at AAC paste, mortar and concrete levels.

At paste level, the pore structure exhibits heterogenous characteristics, which can be significantly influenced by the dispersion of unreacted particles. In low-calcium AAC system, the unreacted fly ash particles can not only introduce interior pores with hollow structures but also trigger the propagation and localisation of micro-cracks at the interfacial transition zone between remnant particles and reaction products [31, 183-185]. Compared with AAMK, AAF shows a wider range and less homogeneous pore size distribution [182, 186]. Due to the higher water-to-binder ratio required for AAMK, AAF also exhibits a lower proportion of pores at the micro level [187]. The pore structure can be altered by the calcium content in AAC. For the Ca-rich AAS paste, the mean pore size and overall porosity tend to be lower in comparison with those of AAF, resulting from the mitigation of large pores since slag can impede the merging of bubbles in matrix [182, 185, 188, 189]. Regarding the blended system, the increase of slag content to no less than 50% in AAFS exhibits a noticeable reduction in porosity with rising tortuosity. Higher slag content can lead to the dominance of the space-filling C-A-S-H gels rather than N-A-S-H gels, which affects the formation of pore network with reduced permeability in AAFS [43, 185]. **Fig. 14** shows the SEM images of AAFS with increasing slag content from 0 to 100%. When subjected to elevated temperatures from 20 to 800 °C, the pore structure can experience a drastic change with increasing porosity by approximately 71%, accounting for 24% of the total volume of AAFS paste [119]. The pore structure evolution in AAC at high temperatures can be associated with the damage mechanisms including further geopolymerisation, pore pressure accumulation, thermal gradient, phase decomposition, recrystallisation and viscous sintering [24, 71, 190-192].

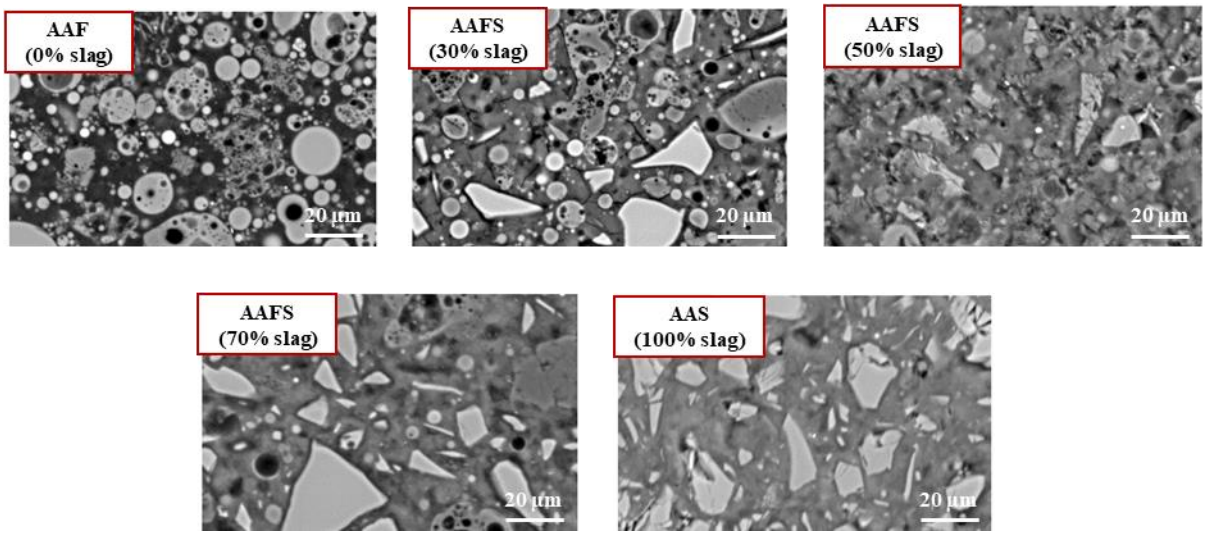

Fig. 14. Microstructural features of AAF, AAS and AAFS with increasing slag content from 30% to 70% [193].

5.4. Microstructure-mechanical property relationships in paste

The relationships between microstructural features and mechanical properties of AAM can be summarised from gel matrix at Level I to paste at Level II. At Level I, the factors that affect the micromechanical performance of gel matrix are mainly associated with two aspects: solid gel particles from Level 0 and gel pores [43]. Considering different types of AAM paste, the evolution of compressive strength in AAF, AAS, AAMK and AAFS from 1 to 28 d is demonstrated in **Fig. 15**. As seen in **Fig. 15(a-c)**, the overall trend of compressive strength shows a continuous rise in single precursor systems at up to 28 d. For low-calcium AAF and AAMK pastes, the 28 d compressive strengths are in the ranges of around 8-54 and 30-66 MPa, respectively. AAS paste exhibits a higher compressive strength of approximately 75-85 MPa at 28 d, while the compressive strength of AAFS paste is highly dependent on the inclusion of slag, indicating a broad range from around 30 to 100 MPa at 28 d (**Fig. 15(d)**). This can be attributed to the effect of chemical compositions, internal structure, phase transformation and gel porosity on the micromechanical properties of gel matrix and compressive strength of paste in AAM.

Firstly, the chemical compositions were found to influence the elastic modulus of different binder gels. For AAF paste, a higher Si/Al ratio can lead to the increase of elastic modulus of N-A-S-H gels, as the bond strength of Si-O bonds are higher than that of Al-O bonds [121, 130]. With different types of alkaline activators, the degree of dissolution can be modified in gel matrix that results in the change of local elastic modulus in the heterogenous structure. In AAS paste, the volume fraction of C-A-S-H gels was reported to increase from 47.3% to 68.0% when replacing SS by SH as the alkaline activator, which indicates a faster reaction and formation of microstructure features with the use of SH, resulting in a more rapid strength development within the gel structure [151] Secondly, the internal structure referring to level of disorder can also influence the micromechanical properties of different types of gel. Comparing with N-A-S-H gels, C-A-S-H gels were observed to contain hints of crystalline phase with order structure. Correspondingly, they exhibit a lower level of disorder with a higher elastic modulus (35-47 GPa) than N-A-S-H gels (11-20 GPa), since N-A-S-H gels possess highly cross-linked amorphous structure with a more pronounced level of disorder [43, 148, 194]. For AAFS, N-C-A-S-H gels have a level of disorder in between C-A-S-H and N-A-S-H gels, which corresponds to the elastic modulus of around 19-23 GPa [25]. Therefore, the phase transformation between different binder gels within gel matrix can be crucial for the micromechanical performance of AAFS [25]. This suggests that the N-C-A-S-H gels can be formed by the exchange of Ca and Na from the original N-A-S-H gels, leading to the change of volume fractions of different reaction products and thus the modification of micromechanical properties [52]. Finally, among the mentioned three types of gel matrix, N-A-S-H gels exhibit the most porous structure, whereas C-A-S-H gels are

the most compact phase with the greatest gel density [37]. This implies that a lower gel porosity can contribute to better micromechanical properties of gel matrix in AAM.

The mechanical properties can be associated with the dissolution of unreacted particles, microstructural properties of different reaction products from Level I and overall pore structure. Regarding unreacted particles, the discrepancy in mechanical properties between fly ash and slag is induced by physical chemistry and degree of dissolution, with elastic modulus of around 72 and 49 GPa, respectively. For reaction products, the phase assemblage of binder gels can significantly contribute to the mechanical properties, influenced by factors such as slag content (i.e., Ca-rich precursors), alkalinity and type of alkaline activators and curing conditions. Regarding pore structure, AAS has lower porosity compared to AAF as the merging of bubbles in paste tends to be impeded by slag [206].

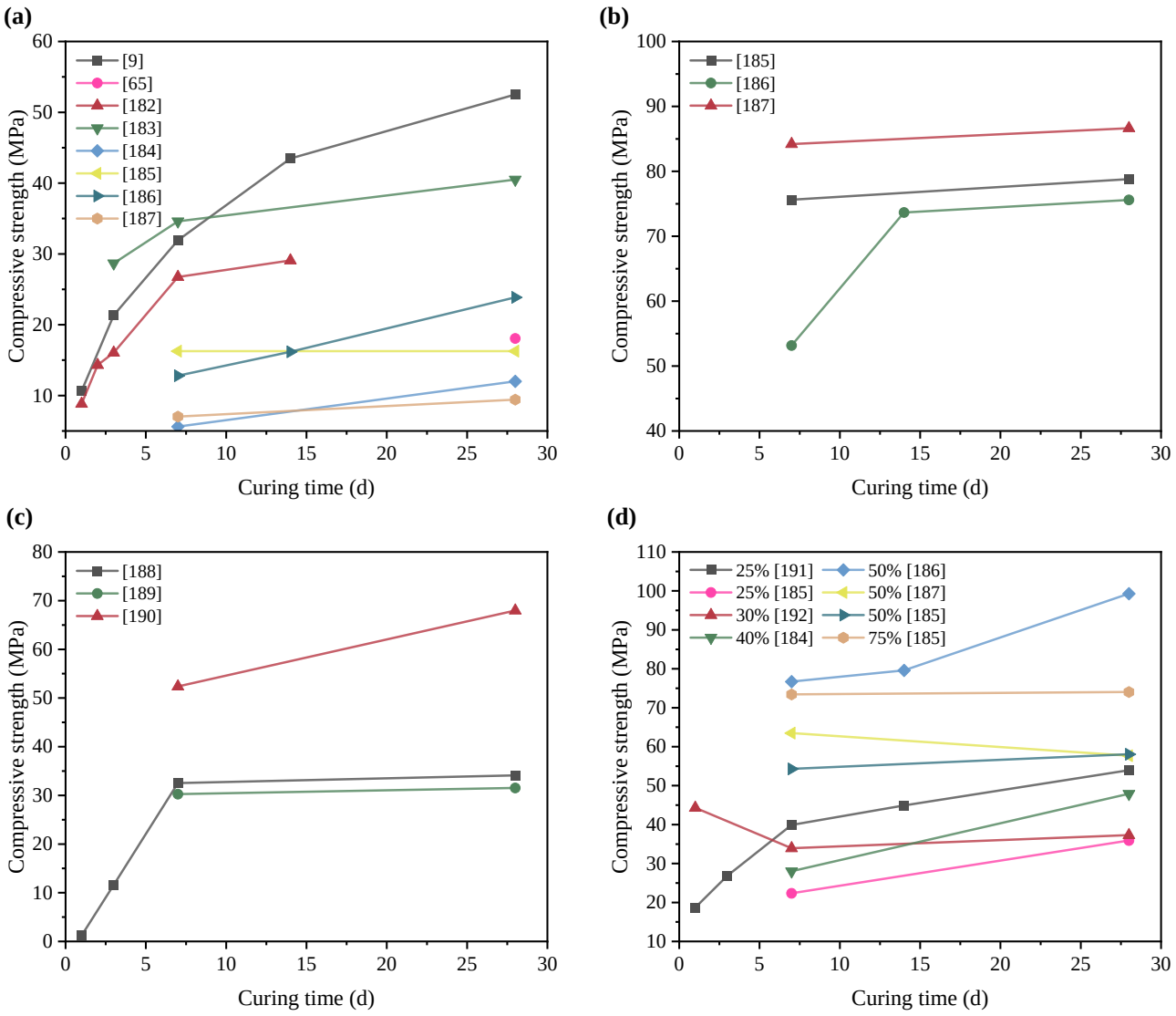

Fig. 15. Compressive strength of different types of paste: (a) AAF [9, 71, 195-200], (b) AAS [198-200], (c) AAMK [201-203], and (d) AAFS with various slag contents [197-200, 204, 205].

6. Level III: Mortar and concrete

The AAM mortar and concrete consists of paste (discussed in Level II), aggregate and ITZ between them. Herein, the microstructural characteristics and micromechanical properties of ITZ in AAC are reviewed, along with a summary of macroscopic performance of AAM mortar (with fine aggregates) and concrete (with both fine and coarse aggregates).

6.1. Interfacial transition zone (ITZ)

6.1.1. Microstructure

ITZ is defined as the interlayer between aggregate and bulk paste and considered as one of the most essential phases that can be responsible for the development of micro-cracks in concrete subjected to loading, affecting the macroscopic properties of cementitious materials [207-210]. In AAF, a well-formed layer of ITZ with dense and uniform structure can be observed at high magnifications 20,000×, which adheres to the surface of aggregate due to wall effect and bonding [210]. **Fig. 16** displays the evolution of ITZ in AAFS at different curing ages from 3 h to 28 d. The ITZ morphology exhibits the occurrence of microcracks, which can be distinguished as bond cracks that develop in between aggregates and bulk paste, and matrix cracks that propagate from aggregate edges towards paste [43, 211]. A major bond crack appears in ITZ after 3 h curing. The formation and propagation of bond cracks within ITZ can be ascribed to the different deformation behaviour between aggregates and paste. As the curing time increases, a tighter bonding between the two phases can be observed, while the bond crack is gradually healed in ITZ by further formation of reaction products. At the curing ages of 3 to 28 d, the formation of matrix cracks can be identified, owing to the different gel compositions and shrinkage performance [212, 213].

Therefore, for reaction products, the EDS results provide the element distribution in ITZ, which can distinctly identify the boundary between aggregates (dominated by calcium) and ITZ (distribution of Na, Al and Si) [210]. The chemical composition in ITZ at up to 28 d is summarised in the ternary diagram in **Fig. 17(a)** based on the element analysis results. A typical ITZ in AAC can consist of high gel content by more than 65% with the layer thickness of 30 μm [210]. The ITZ in AAFS tends to be associated with low-calcium C-(N)-A-S-H gels (Ca/Si ratio from around 0.2 to 0.4) instead of N-A-S-H (Ca/Si ratio < 0.15) from 3 to 12 h, owing to the inclusion of Ca that impedes the formation of N-A-S-H [52, 174]. With the further dissolution of fly ash and slag particles, the reaction products in ITZ cluster more in high-calcium C-(N)-A-S-H and C-A-S-H regions. It is noteworthy that the formation of ITZ may be affected by crystallisation in AAM, as the unreacted particles and their crystals can be low in the vicinity of aggregates due to the wall effect [210, 212, 214, 215]. **Fig. 17(b)** shows the overall porosity and porosity within ITZ and bulk paste, indicating a relatively higher porosity of bulk paste than ITZ at 3 h to 28 d. There exists a significant discrepancy of approximately

3.5% at 3 h, which drops rapidly until 1 d. This can be attributed to the formation of reaction products in bulk paste that significantly refines the pore structure from 12 h to 1 d [25].

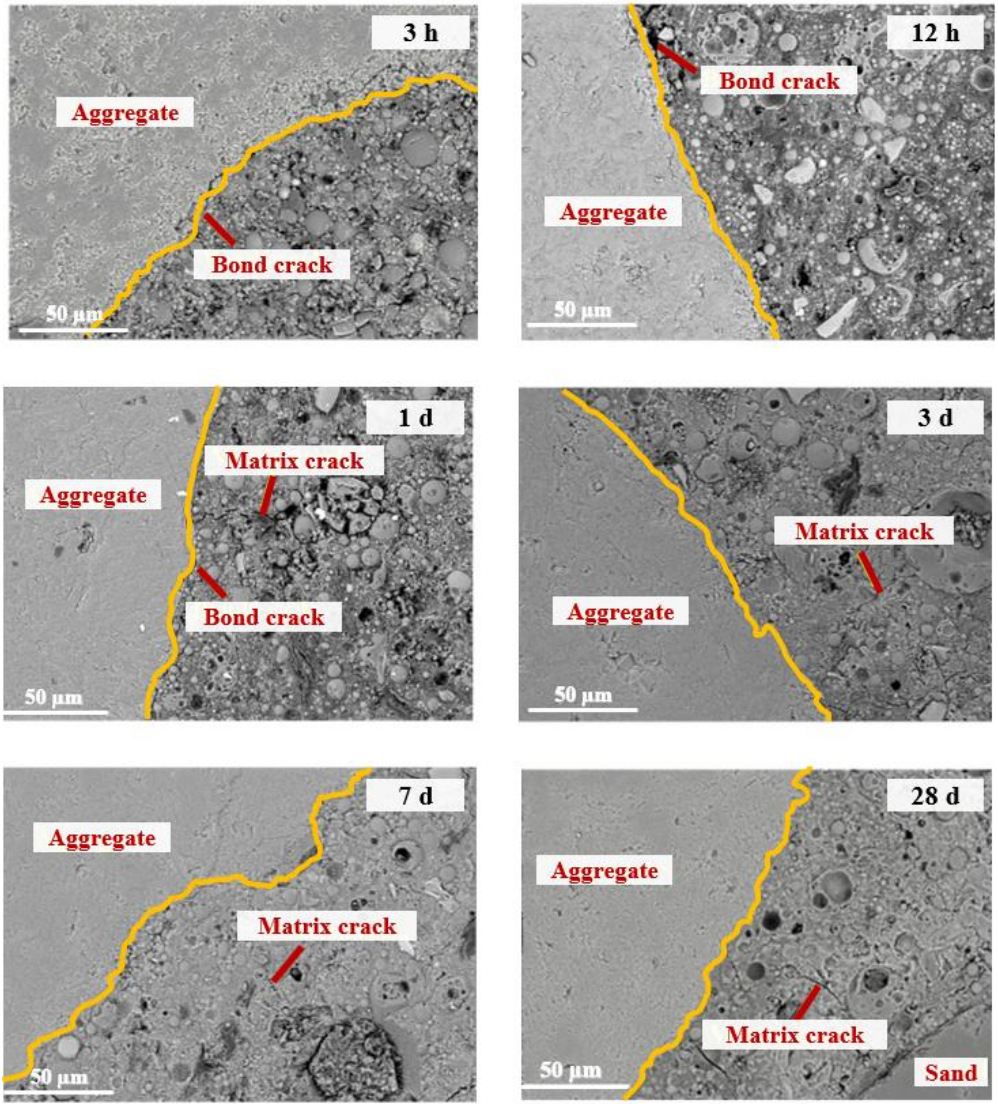

Fig. 16. Morphology of ITZ in AAFS at different curing ages (Adapted from Ref. [43]).

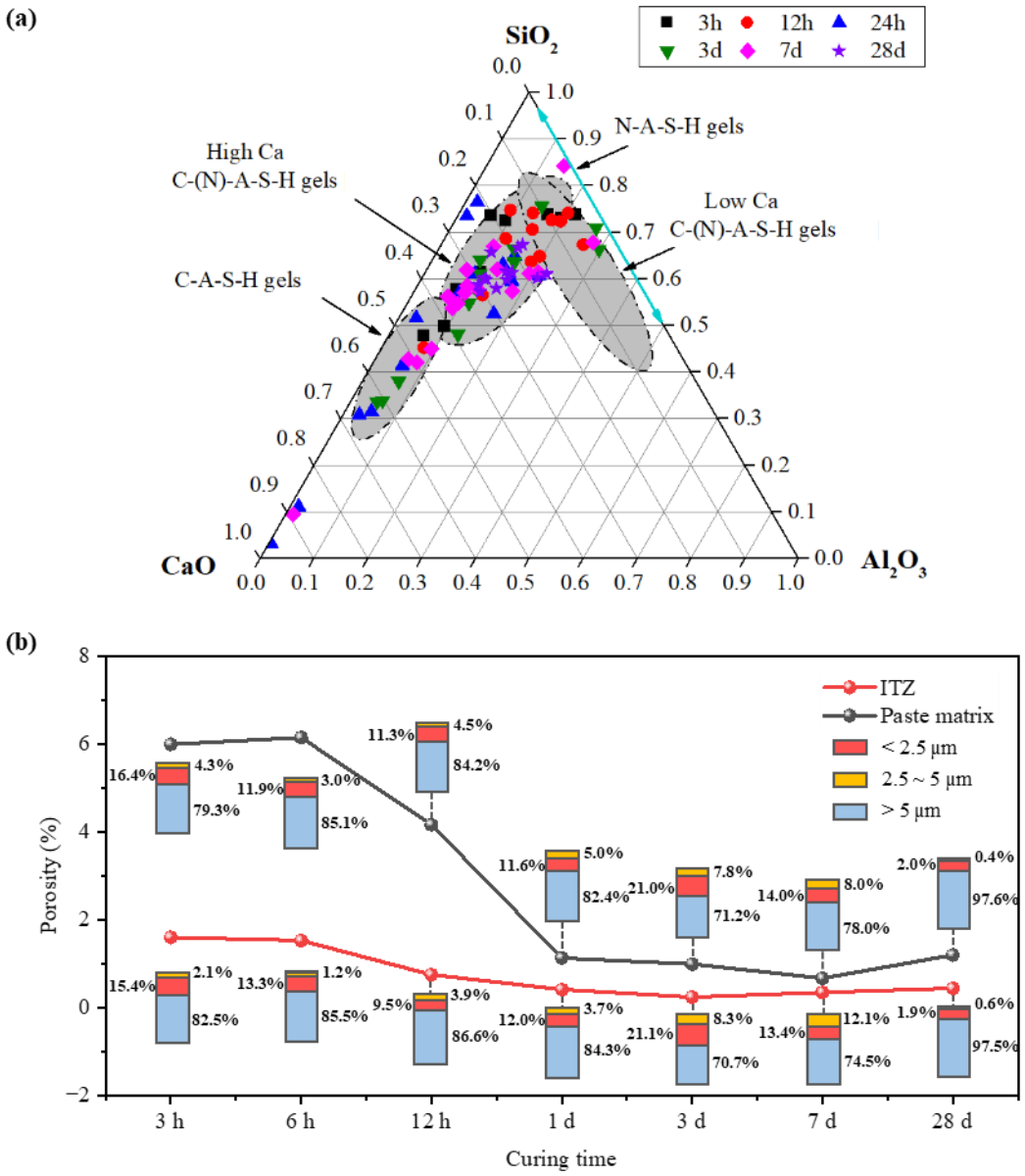

Fig. 17. Microstructural evolution of ITZ at different curing ages: (a) chemical compositions, and (b) overall porosity and volume fractions of pores with diverse sizes, including < 2.5, 2.5~5 and > 5 μm (Adapted from Refs. [25, 43]).

6.1.2. Micromechanical properties

The micromechanical properties of ITZ can be highly associated with the gel compositions, reaction products, pore structure and other factors that modify aggregates and bulk paste in AAC. To enable the comparison between ITZ and paste with respect to micromechanical properties, different techniques such as nanoindentation and nanoscratch have been employed in the previous studies to explore the mechanical responses and heterogeneity of ITZ in AAC [43, 212, 213, 215-221]. Nanoindentation is adopted to investigate the localised ITZ regions, whereas nanoscratch can provide the overall information of ITZ surrounded by different aggregate surfaces [209, 212, 222]. Compared with AAF bulk paste, the comparable mechanical properties obtained in ITZ can be associated with the formation of N-A-S-H gels that provide a strong bond between aggregate and bulk paste [43, 217,

223]. In AAF, the elastic modulus and hardness of ITZ typically range from 17.2-36.7 GPa and 0.76-1.78 GPa, respectively, depending on the locations of ITZ referring to top, bottom and lateral positions, as shown in **Fig. 18(a)** [212]. ITZ at the top surface of aggregate exhibits the highest elastic modulus and hardness, while ITZ at the lateral surface of aggregate has the worst micromechanical properties. the micromechanical properties of ITZ in AAS are dependent on the alkaline activators, in which the mean hardness of ITZ is 76.8% of that of AAS paste [221, 224]. In particular, the use of SS in AAS can introduce excess SiO_2, which potentially boosts the formation of C-A-S-H gels and refine the pore structure in ITZ [154, 220]. Thus, the ITZ in AAS activated by SS exhibits great mechanical properties with low porosity [154, 225].

The micromechanical properties of AAFS are influenced by the evolution of reaction products and microstructural characteristics against curing age [226]. **Fig. 18(b)** illustrates the comparisons of elastic modulus between ITZ and AAFS paste with the evolution of reaction products over curing age at up to 28 d. As the micromechanical properties are dependent on the nature of binder gels in terms of packing density, structure disorder and gel porosity, the elastic modulus of C-A-S-H gels was found to be the highest, followed by N-C-A-S-H and N-A-S-H gels [35, 37]. Hence, the increase of N-C-A-S-H and C-A-S-H gels in ITZ can lead to a comparative growth of elastic modulus by 57% to around 21.2 GPa after 12 h curing, as seen in **Fig. 18(b)**. This can be attributed to the high reactivity of slag that results in the more rapid dissolution of Ca and thus the formation of C-A-S-H gels [227-230]. In addition, according to the aforementioned porosity in ITZ at various curing ages, the decrease of porosity at up to 12 h curing can also contribute to the development of elastic modulus within ITZ, resulted from the refinement of initial microcracks and thus enhance the ITZ structure to provide better micromechanical response. After 28 d of curing, the elastic modulus of ITZ in AAFS can eventually stabilise at approximately 13.2 GPa [226]. Compared with AAFS paste, ITZ exhibits a more compact microstructure with higher elastic modulus at up to 28 d of curing, implying a stronger interfacial bonding between aggregates and bulk paste in AAC compared to traditional PC concrete [231-233]. Since the reaction products and microstructural morphology play crucial roles in the determination of micromechanical properties, it is necessary to explore the modification of AAFS matrix with different slag contents in the future.

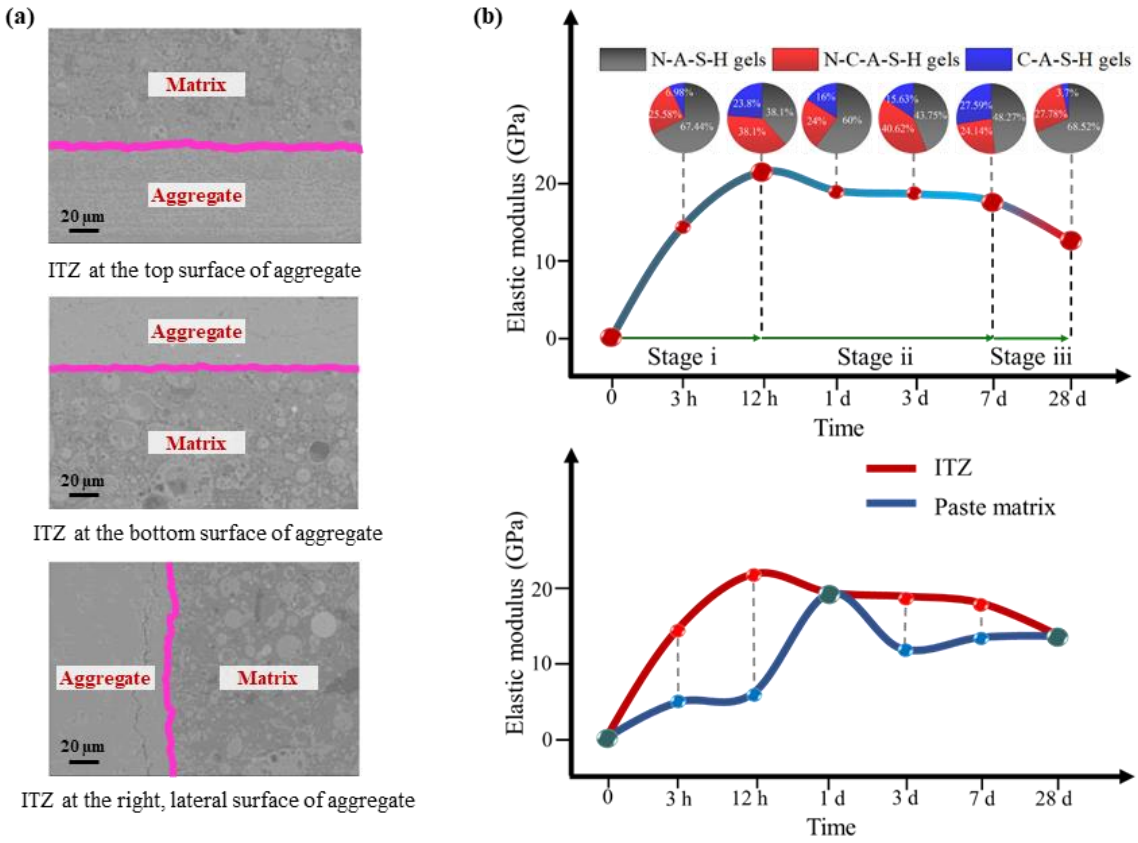

Fig. 18. (a) Different positions of ITZ related to aggregates, and (b) Evolution of elastic modulus in ITZ and bulk paste in AAFS (Adapted from Refs. [25, 212]).

6.2. Microstructure-mechanical property relationships in mortar/concrete

With the inclusion of fine and coarse aggregates, the mechanical properties in terms of strength and stiffness of AAC at Level III are closely associated with the paste and ITZ, especially their microstructural features including chemical compositions and phase assemblage among N-A-S-H, C-A-S-H and N-C-A-S-H [206]. The macroscopic mechanical properties of AAM mortar and concrete including compressive, splitting tensile and flexural strengths have been extensively investigated and summarised in pervious reviews which indicate the importance of alkaline activators, type of precursors, liquid/binder ratios, binder/sand ratios and curing regime [6, 95, 234-236]. **Fig. 19** demonstrates the compressive strength of AAC. In general, all four types of AAC experience continuous strength gain as the curing time increases from 1 to 28 d. At least 80% of compressive strength can be achieved within 7 d of curing in almost all types of AAC, attributed to the fast reaction process and early development of geopolymeric network. The progressive strength growth from 7 to 28 d in AAC is related to further reaction and rearrangement of gel structure towards a stable status with the increasing curing age.

For AAF mortar and concrete, the compressive strength is mostly in the range of 5- 30 MPa at 28 d, depending on different factors. For instance, elevated curing at around 80-90 °C can shorten the time to achieve the ultimate compressive strength by reaching 90% of the total strength within the

first few hours of mixing [234]. Upon heating at higher temperatures of up to 400 °C, the compressive strength of AAF can be enhanced by further geopolymerisation, which can reach up to around 160% of the original strength at 20 °C [31, 249, 250]. AAS mortar and concrete exhibit better compressive strength than AAF, which can reach up to about 80 and 52 MPa at ambient temperature, respectively (**Fig. 19(b)**). However, they exhibit worse high-temperature resistance compared to AAF, due to the decomposition of calcium carbonate at up to 600 °C [22, 23, 251]. The compressive strength of AAFS is dependent on the slag content. As seen in **Fig. 19(d)**, when the slag content rises from 10% to 30% in AAFS concrete, the compressive strength can be enhanced from 28 MPa to around 60 MPa at 28 d of curing [3, 43]. Therefore, the compositions of unreacted particles, phase assemblage of reaction products and propagation of cracks can be crucial to the development of compressive strength, depending on the mix design of AAFS paste and selection of fine and coarse aggregates. The static mechanical properties of AAC have been systematically studied, while the dynamic properties of AAC linking to microstructural evolution and micromechanical properties have been rarely explored.

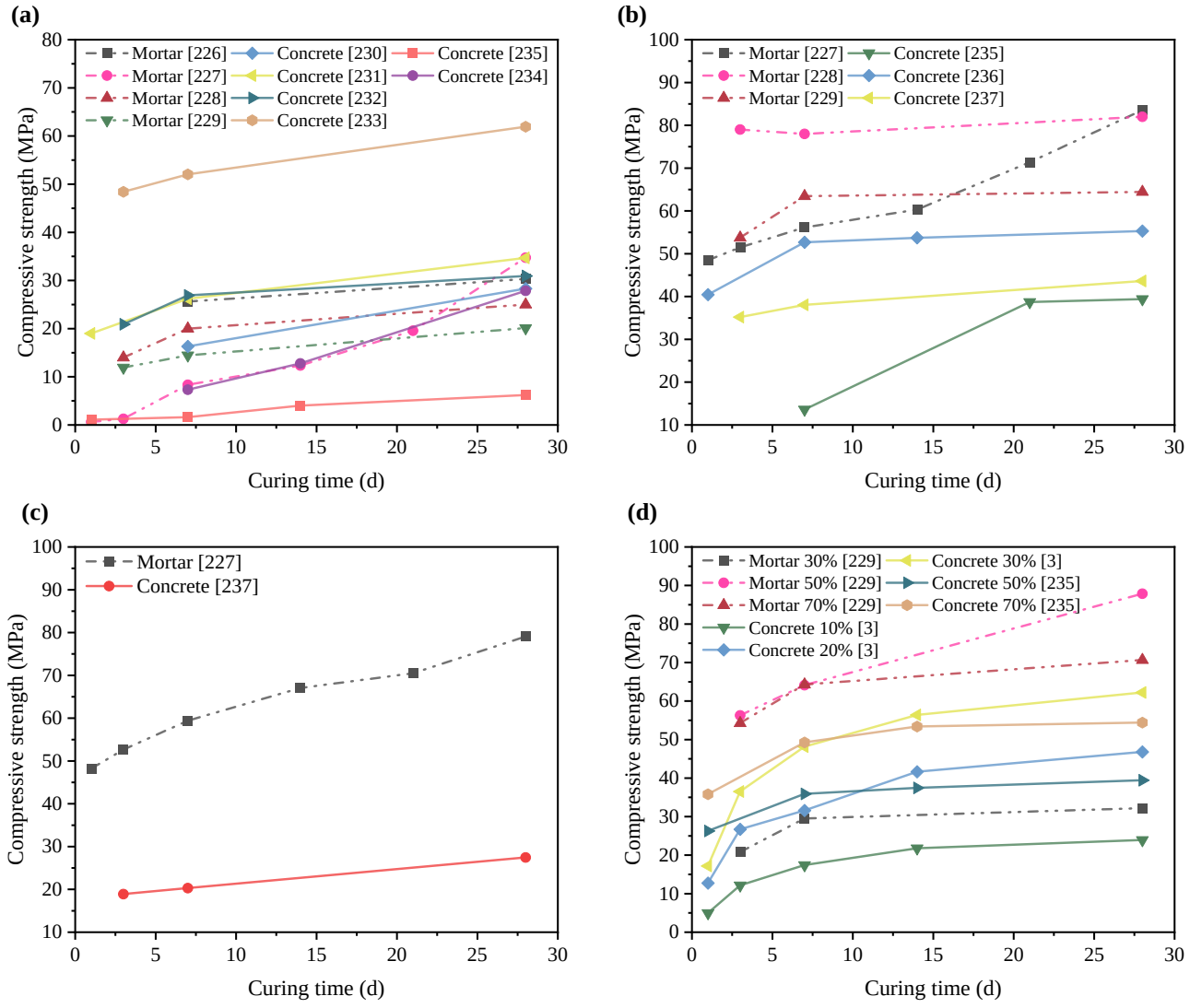

Fig. 19. Compressive strengths of different types of AAC: (a) AAF [237-246], (b) AAS [238-240, 246-248], (c) AAMK [238, 248], and (d) AAFS with various slag contents [3, 240, 246].

7. Conclusions and perspectives

7.1. Conclusions

This paper provides a systematic summary of the microstructure and micromechanical properties of AAC from nano-scale to macro-scale, with respect to Level 0 (N-A-S-H, C-A-S-H and N-C-A-S-H solid gel particles), Level I (gel matrix), Level II (paste: unreacted particles, reaction products and pores), and Level III (ITZ, mortar and concrete). Some main conclusions can be drawn as follows:

- Regarding single precursor systems such as AAF, AAS and AAMK, the reaction process consists of different steps, including dissolution of precursors, rearrangement, gelation and solidification to form N-A-S-H gels in low-calcium AAF and C-A-S-H gels in high-calcium AAS. As for blend precursor system, the hybrid N-C-A-S-H gels are formed in AAFS due to the local chemical interactions between different precursors during alkaline activations, leading to the heterogeneity of composition distribution in the microstructure.
- N-A-S-H gels exhibit 3D networks with a silicon tetrahedron connecting to other three tetrahedrons, which can be transferred from Al-rich to Si-rich with increasing curing time. C-A-S-H gels are formed of silicate chains interlinked by layers of CaO. The formation of N-C-A-S-H gels is induced by the partial replacement of Na^+ by free Ca^{2+} in N-A-S-H gels. This hybrid gel exhibits mineral characteristics that bridge the gap between the other two mentioned above, which can both maintain the inherent 3D aluminosilicate framework like N-A-S-H and possess a composition similar to that of C-A-S-H. The phase transformation between N-(C)-A-S-H and C-A-S-H gels can be associated with a critical pH of 12.
- The elastics modulus of different reaction products in AAC follows an order of N-A-S-H gels (11-20 GPa) < N-C-A-S-H gels (19-23 GPa) < C-A-S-H gels (35-47 GPa), which strongly affects the macroscopic mechanical strengths of AAF, AAS and AAFS. For unreacted precursors, the dissolution of particles took place, followed by the formation of surrounding reaction products with the rupture of Si-O-Si and Al-O-Al bonds in fly ash and Ca-O and Si-O-Si bonds in slag. The elastic modulus of unreacted fly ash and slag particles vary between 30-140 GPa and 46-70 GPa, respectively.
- The pore structure exhibits heterogenous characteristics at paste level, depending on the factors like dispersion of unreacted particles and exposure temperatures. A rise in porosity by up to 71% can be found in AAFS paste at 28 d when increasing the curing temperature from 20 to 800 °C.
- The morphology of ITZ in AAC is dependent on curing time, since the observed bond crack in AAFS after 3 h of mixing can be healed when the curing time reaches 3 d. The micromechanical characteristics of ITZ in AAC are determined by the evolution of reaction products in ITZ as time goes by, which can stabilise at around 13.2 GPa after 28 d of curing.

- In general, the mechanical properties of AAC in both single and blend precursor systems are closely related to the microstructural features. The increase of cross-linking level of binder gels (N-A-S-H > N-C-A-S-H > C-A-S-H) in different reaction products corresponds to the 28 d strength of different types of AAC (AAF < AAFS < AAS).

7.2. Perspectives

For future engineering applications of AAC and practical use in sustainable infrastructure design, the following aspects need to be considered based on the existing research gaps: (1) The evolution of phase compositions in AAF, AAMK and AAS with increasing curing time can be investigated to link the mechanical properties with microstructural changes in different types of AAC. (2) The multiscale microstructural characteristics and damage evolution in different types of AAC subjected to hazards such as fire/high temperatures, freeze-thaw cycles and dynamic loading can be explored. (3) More studies on the use of greener precursors, eco-friendly alkaline activators and recycled reinforcing materials (e.g., recycled fibres) to develop sustainable high-performance AAC are required for sustainable and resilient civil infrastructure.

Acknowledgements

The financial support provided by University College London (UCL) through a Graduate Research Scholarship to the first author is greatly appreciated.

References

[1] C.J. Shi, A.F. Jimenez, A. Palomo, New cements for the 21st century: The pursuit of an alternative to Portland cement, Cement Concrete Res, 41 (2011) 750-763.

[2] J.L. Provis, S.A. Bernal, Geopolymers and Related Alkali-Activated Materials, Annu Rev Mater Res, 44 (2014) 299-327.

[3] G.H. Fang, W.K. Ho, W.L. Tu, M.Z. Zhang, Workability and mechanical properties of alkali-activated fly ash-slag concrete cured at ambient temperature, Constr Build Mater, 172 (2018) 476-487.

[4] Y. Ma, G. Ye, The shrinkage of alkali activated fly ash, Cement Concrete Res, 68 (2015) 75-82.

[5] C. Gunasekara, D.W. Law, S. Setunge, J.G. Sanjayan, Zeta potential, gel formation and compressive strength of low calcium fly ash geopolymers, Constr Build Mater, 95 (2015) 592-599.

[6] P. Zhang, X.Y. Sun, F. Wang, J. Wang, Mechanical Properties and Durability of Geopolymer Recycled Aggregate Concrete: A Review, Polymers-Basel, 15 (2023) 615.

[7] K. Korniejenko, P. Kejzlar, P. Louda, The Influence of the Material Structure on the Mechanical Properties of Geopolymer Composites Reinforced with Short Fibers Obtained with Additive Technologies, Int J Mol Sci, 23 (2022) 2023.

[8] Z. Gao, P. Zhang, J.J. Guo, K.X. Wang, Bonding behavior of concrete matrix and alkali-activated mortar incorporating nano-SiO2 and polyvinyl alcohol fiber: Theoretical analysis and prediction model, Ceram Int, 47 (2021) 31638-31649.
[9] M. Hanumananaik, K.V.L. Subramaniam, Shrinkage in low-calcium fly ash geopolymers for precast applications: Reaction product content and pore structure under drying conditions, J Build Eng, 78 (2023) 107583.
[10] A. Fakhrabadi, A.J. Choobbasti, S.S. Kutanaei, Durability Evaluation of Clayey Sandy Soil Stabilized with Copper-Slag-Based Geopolymer Under Freezing-Thawing Cycles, Int J Pavement Res T, (2023) 1-18.
[11] Z. Azimi, V. Toufigh, Influence of Blast Furnace Slag on Pore Structure and Transport Characteristics in Low-Calcium Fly-Ash-Based Geopolymer Concrete, Sustainability-Basel, 15 (2023) 13348.
[12] F. Hong, S. Yu, D.S. Hou, Z.J. Li, H.W. Sun, P. Wang, M.H. Wang, Study on the mechanical properties, gelling products and alkalization process of alkali-activated metakaolin: From experiment to molecular dynamics simulation, J Build Eng, 79 (2023) 107705.
[13] B. Zhang, H. Zhu, P. Feng, P. Zhang, A review on shrinkage-reducing methods and mechanisms of alkali-activated/geopolymer systems: Effects of chemical additives, J Build Eng, 49 (2022) 104056.
[14] S.Y. Guo, Y.L. Wu, Z.Q. Jia, X.Q. Qi, W.R. Wang, Sodium-based activators in alkali- activated materials: Classification and comparison, J Build Eng, 70 (2023) 106397.
[15] A. Erfanimanesh, M.K. Sharbatdar, Mechanical and microstructural characteristics of geopolymer paste, mortar, and concrete containing local zeolite and slag activated by sodium carbonate, J Build Eng, 32 (2020) 101781.
[16] Y. Essam, N. El-Faramawy, W. Ramadan, M. Ramadan, From dangerous wastes to green construction materials, as thermally stable-radiation blocker, in presence of meso-porous magnesia and alumina, J Build Eng, 66 (2023) 105896.
[17] Y.R. Wang, Y.B. Cao, Z.H. Zhang, P. Zhang, Y.W. Ma, A.G. Wang, H. Wang, Intrinsic sulfuric acid resistance of C-(N)-A-S-H and N-A-S-H gels produced by alkali-activation of synthetic calcium aluminosilicate precursors, Cement Concrete Res, 165 (2023) 107068.
[18] I. Nikolic, L. Karanovic, I.J. Castvan, V. Radmilovic, S. Mentus, V. Radmilovic, Improved compressive strength of alkali activated slag upon heating, Mater Lett, 133 (2014) 251-254.
[19] H.H. Chen, A. Nikvar-Hassani, S. Ormsby, D. Ramey, L.Y. Zhang, Mechanical and microstructural investigations on the low-reactive copper mine tailing-based geopolymer activated by phosphoric acid, Constr Build Mater, 393 (2023) 132030.
[20] M. Hanumananaik, K.V.L. Subramaniam, Influence of Process Variables on Shrinkage in Low-Calcium Fly-Ash Geopolymers, J Mater Civil Eng, 35 (2023) 04023143.

[21] C.H. Xue, V. Sirivivatnanon, A. Nezhad, Q.X. Zhao, Comparisons of alkali-activated binder concrete (ABC) with OPC concrete-A review, Cement Concrete Comp, 135 (2023) 104851.
[22] Z. Pan, J.G. Sanjayan, B.V. Rangan, An investigation of the mechanisms for strength gain or loss of geopolymer mortar after exposure to elevated temperature, J Mater Sci, 44 (2009) 1873-1880.
[23] Z. Pan, J.G. Sanjayan, F. Collins, Effect of transient creep on compressive strength of geopolymer concrete for elevated temperature exposure, Cement Concrete Res, 56 (2014) 182-189.
[24] Z. Pan, Z. Tao, Y.F. Cao, R. Wuhrer, T. Murphy, Compressive strength and microstructure of alkali-activated fly ash/slag binders at high temperature, Cement Concrete Comp, 86 (2018) 9-18.
[25] G.H. Fang, M.Z. Zhang, Multiscale micromechanical analysis of alkali-activated fly ash-slag paste, Cement Concrete Res, 135 (2020) 105860.
[26] H.U. Ahmed, A.S. Mohammed, S.M.A. Qaidi, R.H. Faraj, N.H. Sor, A.A. Mohammed, Compressive strength of geopolymer concrete composites: a systematic comprehensive review, analysis and modeling, Eur J Environ Civ En, 27 (2023) 1383-1428.
[27] R. Asghar, M.A. Khan, R. Alyousef, M.F. Javed, M. Ali, Promoting the green Construction: Scientometric review on the mechanical and structural performance of geopolymer concrete, Constr Build Mater, 368 (2023) 130502.
[28] H. Bahmani, D. Mostofinejad, A review of engineering properties of ultra-high-performance geopolymer concrete, Dev Built Environ, 14 (2023) 100126.
[29] A.B. Elhag, A. Raza, Q.U.Z. Khan, M. Abid, B. Masood, M. Arshad, A.F. Deifalla, A critical review on mechanical, durability, and microstructural properties of industrial by-product-based geopolymer composites, Rev Adv Mater Sci, 62 (2023) 20220306.
[30] A. Hassan, M. Arif, M. Shariq, T. Alomayri, S. Pereira, Fire resistance characteristics of geopolymer concrete for environmental sustainability: a review of thermal, mechanical and microstructure properties, Environ Dev Sustain, 25 (2023) 8975-9010.
[31] W.L. Tu, M.Z. Zhang, Behaviour of alkali-activated concrete at elevated temperatures: A critical review, Cement Concrete Comp, 138 (2023) 104961.
[32] F. Puertas, S. Martínez-Ramírez, S. Alonso, T. Vázquez, Alkali-activated fly ash/slag cement -: Strength behaviour and hydration products, Cement Concrete Res, 30 (2000) 1625-1632.
[33] C.L. Hu, Z.J. Li, A review on the mechanical properties of cement-based materials measured by nanoindentation, Constr Build Mater, 90 (2015) 80-90.
[34] V. Smilauer, P. Hlavacek, F. Skvara, R. Sulc, L. Kopecky, J. Nemecek, Micromechanical multiscale model for alkali activation of fly ash and metakaolin, J Mater Sci, 46 (2011) 6545-6555.
[35] R.J. Thomas, B.S. Gebregziabiher, A. Giffin, S. Peethamparan, Micromechanical properties of alkali-activated slag cement binders, Cement Concrete Comp, 90 (2018) 241-256.

[36] J. Nemecek, V. Smilauer, L. Kopecky, Characterization of Alkali-Activated Fly-Ash by Nanoindentation, Nanotechnology in Construction 3, Proceedings, (2009) 337-343.
[37] J. Nemecek, V. Smilauer, L. Kopecky, Nanoindentation characteristics of alkali-activated aluminosilicate materials, Cement Concrete Comp, 33 (2011) 163-170.
[38] H. Lee, V. Vimonsatit, P. Chindaprasirt, Mechanical and micromechanical properties of alkali activated fly-ash cement based on nano-indentation, Constr Build Mater, 107 (2016) 95-102.
[39] Y. Ma, G. Ye, J. Hu, Micro-mechanical properties of alkali-activated fly ash evaluated by nanoindentation, Constr Build Mater, 147 (2017) 407-416.
[40] F. Puertas, M. Palacios, H. Manzano, J.S. Dolado, A. Rico, J. Rodriguez, A model for the C-A-S-H gel formed in alkali-activated slag cements, J Eur Ceram Soc, 31 (2011) 2043-2056.
[41] G. Constantinides, F.J. Ulm, The effect of two types of C-S-H on the elasticity of cement-based materials: Results from nanoindentation and micromechanical modeling, Cement Concrete Res, 34 (2004) 67-80.
[42] H.M. Jennings, J.J. Thomas, J.S. Gevrenov, G. Constantinides, F.J. Ulm, A multi-technique investigation of the nanoporosity of cement paste - Reply, Cement Concrete Res, 37 (2007) 1374-1375.
[43] G. Fang, Multiscale Characterisation of Microstructure and Mechanical Properties of Alkali-Activated Fly Ash-Slag Concrete, UCL (University College London), 2021.
[44] C. Li, H.H. Sun, L.T. Li, A review: The comparison between alkali-activated slag (Si plus Ca) and metakaolin (Si plus Al) cements, Cement Concrete Res, 40 (2010) 1341-1349.
[45] Z.Q. Sun, A. Vollpracht, Isothermal calorimetry and in-situ XRD study of the NaOH activated fly ash, metakaolin and slag, Cement Concrete Res, 103 (2018) 110-122.
[46] I. Ismail, S.A. Bernal, J.L. Provis, R.S. Nicolas, S. Hamdan, J.S.J. van Deventer, Modification of phase evolution in alkali-activated blast furnace slag by the incorporation of fly ash, Cement Concrete Comp, 45 (2014) 125-135.
[47] A. Palomo, P. Krivenko, I. Garcia-Lodeiro, E. Kavalerova, O. Maltseva, A. Fernandez-Jimeneza, A review on alkaline activation: new analytical perspectives, Mater Construcc, 64 (2014) 22.
[48] B. Liu, C.Y. Zhu, K.D. Zhuang, L. Shuai, D.X. Li, W.J. Long, F. Xing, Y. Fang, Insights into the Microstructure of Hydrothermal Synthesized Nanoscale KO-AlO-SiO-HO Particles, Nanomaterials-Basel, 10 (2020) 10010063.
[49] T.T.H. Bach, E. Chabas, I. Pochard, C.C.D. Coumes, J. Haas, F. Frizon, A. Nonat, Retention of alkali ions by hydrated low-pH cements: Mechanism and Na/K selectivity, Cement Concrete Res, 51 (2013) 14-21.
[50] T.T.H. Bach, C.C.D. Coumes, I. Pochard, C. Mercier, B. Revel, A. Nonat, Influence of temperature on the hydration products of low pH cements, Cement Concrete Res, 42 (2012) 805-817.

[51] N.K. Lee, H.K. Lee, Reactivity and reaction products of alkali-activated, fly ash/slag paste, Constr Build Mater, 81 (2015) 303-312.
[52] I. Garcia-Lodeiro, A. Palomo, A. Fernandez-Jimenez, D.E. Macphee, Compatibility studies between N-A-S-H and C-A-S-H gels. Study in the ternary diagram Na2O-CaO-Al2O3-SiO2-H2O, Cement Concrete Res, 41 (2011) 923-931.
[53] H.L. Ye, A. Radlinska, Fly ash-slag interaction during alkaline activation: Influence of activators on phase assemblage and microstructure formation, Constr Build Mater, 122 (2016) 594-606.
[54] I. Garcia-Lodeiro, A. Fernandez-Jimenez, A. Palomo, Variation in hybrid cements over time. Alkaline activation of fly ash-portland cement blends, Cement Concrete Res, 52 (2013) 112-122.
[55] D.S. Hou, W. Zhang, J. Sun, J.G. Zhang, Structure, dynamics and mechanical properties evolution of calcium-silicate-hydrate induced by Fe ions: A molecular dynamics study, Constr Build Mater, 287 (2021) 122875.
[56] A. Mancini, E. Wieland, G. Geng, R. Dähn, J. Skibsted, B. Wehrli, B. Lothenbach, Fe(III) uptake by calcium silicate hydrates, Appl Geochem, 113 (2020) 104460.
[57] Y. Fang, K.D. Zhuang, H.Z. Cui, Z.H. Zhang, A.X. Wang, C.M. Wang, D.P. Zheng, X.F. Wang, The state of Fe in the C-F-A-S-H system with varying Fe/Si and Ca/Si ratios, J Mater Chem A, 11 (2023) 26193-26211.
[58] H. Castillo, H. Collado, T. Droguett, M. Vesely, P. Garrido, S. Palma, State of the art of geopolymers: A review, E-Polymers, 22 (2022) 108-124.
[59] Y.S. Wang, Y. Alrefaei, J.G. Dai, Silico-Aluminophosphate and Alkali-Aluminosilicate Geopolymers: A Comparative Review, Front Mater, 6 (2019) 106.
[60] S. Qaidi, H.M. Najm, S.M. Abed, H.U. Ahmed, H. Al Dughaishi, J. Al Lawati, M.M. Sabri, F. Alkhatib, A. Milad, Fly Ash-Based Geopolymer Composites: A Review of the Compressive Strength and Microstructure Analysis, Materials, 15 (2022) 7098.
[61] T. Yang, X. Yao, Z.H. Zhang, H. Wang, Mechanical property and structure of alkali-activated fly ash and slag blends, J Sustain Cem-Based, 1 (2012) 167-178.
[62] A. Fernandez-Jimenez, A. Palomo, I. Sobrados, J. Sanz, The role played by the reactive alumina content in the alkaline activation of fly ashes, Micropor Mesopor Mat, 91 (2006) 111-119.
[63] M. Criado, A. Fernandez-Jimenez, A. Palomo, Alkali activation of fly ash. Part III: Effect of curing conditions on reaction and its graphical description, Fuel, 89 (2010) 3185-3192.
[64] F. Lolli, H. Manzano, J.L. Provis, M.C. Bignozzi, E. Masoero, Atomistic Simulations of Geopolymer Models: The Impact of Disorder on Structure and Mechanics, Acs Appl Mater Inter, 10 (2018) 22809-22820.
[65] S. Le Roux, V. Petkov, ISAACS - interactive structure analysis of amorphous and crystalline systems, J Appl Crystallogr, 43 (2010) 181-185.

[66] S.J. Louisnathan, R.J. Hill, G.V. Gibbs, Tetrahedral Bond Length Variations in Sulfates, Phys Chem Miner, 1 (1977) 53-69.
[67] X.L. Yuan, A. Cormack, Si-O-Si bond angle and torsion angle distribution in vitreous silica and sodium silicate glasses, J Non-Cryst Solids, 319 (2003) 31-43.
[68] G.W. Scherer, Structure and properties of gels, Cement Concrete Res, 29 (1999) 1149-1157.
[69] M. Torres-Carrasco, F. Puertas, Alkaline activation of different aluminosilicates as an alternative to Portland cement: alkali activated cements or geopolymers, Rev Ing Constr, 32 (2017) 5-12.
[70] S.K. Nath, S. Kumar, Role of particle fineness on engineering properties and microstructure of fly ash derived geopolymer, Constr Build Mater, 233 (2020) 117294.
[71] Y. Luo, S.H. Li, K.M. Klima, H.J.H. Brouwers, Q.L. Yu, Degradation mechanism of hybrid fly ash/slag based geopolymers exposed to elevated temperatures, Cement Concrete Res, 151 (2022) 106649.
[72] B. Aouan, S. Alehyen, M. Fadil, M. El Alouani, H. Saufi, M. Taibi, Characteristics, microstructures, and optimization of the geopolymer paste based on three aluminosilicate materials using a mixture design methodology, Constr Build Mater, 384 (2023) 131475.
[73] M. El Alouani, S. Alehyen, H. El Hadki, H. Saufi, A. Elhalil, O.K. Kabbaj, M. Taibi, Synergetic influence between adsorption and photodegradation of Rhodamine B using synthesized fly ash based inorganic polymer, Surf Interfaces, 24 (2021) 101136.
[74] S.Q. Ruan, S.K. Chen, Y.J. Zhang, J.X. Mao, D.M. Yan, Y. Liu, X.F. Liu, H. Hosono, Molecular-Level Hybridized Hydrophobic Geopolymer Ceramics for Corrosion Protection, Chem Mater, (2023) 1735-1744.
[75] F.J. Ulm, G. Constantinides, F.H. Heukamp, Is concrete a poromechanics material? - A multiscale investigation of poroelastic properties, Mater Struct, 37 (2004) 43-58.
[76] J. Yang, D.S. Hou, Q.J. Ding, Structure, Dynamics, and Mechanical Properties of Cross-Linked Calcium Aluminosilicate Hydrate: A Molecular Dynamics Study, Acs Sustain Chem Eng, 6 (2018) 9403-9417.
[77] J. Wongpa, K. Kiattikomol, C. Jaturapitakkul, P. Chindaprasirt, Compressive strength, modulus of elasticity, and water permeability of inorganic polymer concrete, Mater Design, 31 (2010) 4748-4754.
[78] R. Sulc, T. Strnad, F. Skvara, P. Svoboda, Z. Bittnar, V. Smilauer, L. Kopecký, Concrete Based on Fly Ash Alumosilicate Polymers, Journal of Environmental Science and Engineering, 5 (2011) 728-735.
[79] P. Duxson, A. Fernandez-Jimenez, J.L. Provis, G.C. Lukey, A. Palomo, J.S.J. van Deventer, Geopolymer technology: the current state of the art, J Mater Sci, 42 (2007) 2917-2933.

[80] J.S.J. van Deventer, J.L. Provis, P. Duxson, G.C. Lukey, Reaction mechanisms in the geopolymeric conversion of inorganic waste to useful products, J Hazard Mater, 139 (2007) 506-513.
[81] M.J.A. Qomi, F.J. Ulm, R.J.M. Pellenq, Evidence on the Dual Nature of Aluminum in the Calcium-Silicate-Hydrates Based on Atomistic Simulations, J Am Ceram Soc, 95 (2012) 1128-1137.
[82] S.A. Hamid, The Crystal-Structure of the 11-a Natural Tobermorite Ca2.25[Si3O7.5(OH)1.5]]·1H2O Z Kristallogr, 154 (1981) 189-198.
[83] P. Faucon, J.M. Delaye, J. Virlet, J.F. Jacquinot, F. Adenot, Study of the structural properties of the C-S-H(I) by molecular dynamics simulation, Cement Concrete Res, 27 (1997) 1581-1590.
[84] S. Merlino, E. Bonaccorsi, T. Armbruster, The real structure of tobermorite 11 angstrom: normal and anomalous forms, OD character and polytypic modifications, Eur J Mineral, 13 (2001) 577-590.
[85] T. Mitsuda, H.F.W. Taylor, Normal and Anomalous Tobermorites, Mineral Mag, 42 (1978) 229-235.
[86] H. Stade, D. Muller, On the Coordination of Al in Ill-Crystallized C-S-H Phases Formed by Hydration of Tricalcium Silicate and by Precipitation Reactions at Ambient-Temperature, Cement Concrete Res, 17 (1987) 553-561.
[87] P. Faucon, A. Delagrave, J.C. Petit, C. Richet, J.M. Marchand, H. Zanni, Aluminum incorporation in calcium silicate hydrates (C-S-H) depending on their Ca/Si ratio, J Phys Chem B, 103 (1999) 7796-7802.
[88] G.K. Sun, J.F. Young, R.J. Kirkpatrick, The role of Al in C-S-H: NMR, XRD, and compositional results for precipitated samples, Cement Concrete Res, 36 (2006) 18-29.
[89] M.D. Andersen, H.J. Jakobsen, J. Skibsted, Incorporation of aluminum in the calcium silicate hydrate (C-S-H) of hydrated Portland cements: A high-field Al-27 and Si-29 MAS NMR Investigation, Inorg Chem, 42 (2003) 2280-2287.
[90] A. Rawal, B.J. Smith, G.L. Athens, C.L. Edwards, L. Roberts, V. Gupta, B.F. Chmelka, Molecular Silicate and Aluminate Species in Anhydrous and Hydrated Cements, J Am Chem Soc, 132 (2010) 7321-7337.
[91] M.D. Andersen, H.J. Jakobsen, J. Skibsted, A new aluminium-hydrate species in hydrated Portland cements characterized by Al-27 and Si-29 MAS NMR spectroscopy, Cement Concrete Res, 36 (2006) 3-17.
[92] X. Pardal, I. Pochard, A. Nonat, Experimental study of Si-Al substitution in calcium-silicate-hydrate (C-S-H) prepared under equilibrium conditions, Cement Concrete Res, 39 (2009) 637-643.
[93] I.G. Richardson, A.R. Brough, R. Brydson, G.W. Groves, C.M. Dobson, Location of Aluminum in Substituted Calcium Silicate Hydrate (C-S-H) Gels as Determined by Si-29 and Al-27 Nmr and Eels, J Am Ceram Soc, 76 (1993) 2285-2288.

[94] J. Skibsted, M.D. Andersen, The Effect of Alkali Ions on the Incorporation of Aluminum in the Calcium Silicate Hydrate (C-S-H) Phase Resulting from Portland Cement Hydration Studied by Si-29 MAS NMR, J Am Ceram Soc, 96 (2013) 651-656.
[95] A.A. Mohammed, H.U. Ahmed, A. Mosavi, Survey of Mechanical Properties of Geopolymer Concrete: A Comprehensive Review and Data Analysis, Materials, 14 (2021) 4690.
[96] H. Manzano, J.S. Dolado, M. Griebel, J. Hamaekers, A molecular dynamics study of the aluminosilicate chains structure in Al-rich calcium silicate hydrated (C-S-H) gels, Phys Status Solidi A, 205 (2008) 1324-1329.
[97] I.G. Richardson, G.W. Groves, The structure of the calcium silicate hydrate phases present in hardened pastes of white Portland cement blast-furnace slag blends, J Mater Sci, 32 (1997) 4793-4802.
[98] S.A. Bernal, J.L. Provis, B. Walkley, R.S. Nicolas, J.D. Gehman, D.G. Brice, A.R. Kilcullen, P. Duxson, J.S.J. van Deventer, Gel nanostructure in alkali-activated binders based on slag and fly ash, and effects of accelerated carbonation, Cement Concrete Res, 53 (2013) 127-144.
[99] B. Walkley, R. San Nicolas, M.A. Sani, G.J. Rees, J.V. Hanna, J.S.J. van Deventer, J.L. Provis, Phase evolution of C-(N)-A-S-H/N-A-S-H gel blends investigated via alkali-activation of synthetic calcium aluminosilicate precursors, Cement Concrete Res, 89 (2016) 120-135.
[100] E. Kapeluszna, L. Kotwica, A. Rózycka, L. Golek, Incorporation of Al in C-A-S-H gels with various Ca/Si and Al/Si ratio: Microstructural and structural characteristics with DTA/TG, XRD, FTIR and TEM analysis, Constr Build Mater, 155 (2017) 643-653.
[101] P. Chindaprasirt, P. De Silva, K. Sagoe-Crentsil, S. Hanjitsuwan, Effect of SiO2 and Al2O3 on the setting and hardening of high calcium fly ash-based geopolymer systems, J Mater Sci, 47 (2012) 4876-4883.
[102] I. Garcia-Lodeiro, A. Palomo, A. Fernández-Jiménez, An overview of the chemistry of alkali-activated cement-based binders, Handbook of alkali-activated cements, mortars and concretes, (2015) 19-47.
[103] M.R. Ahmad, L.P. Qian, Y. Fang, A.G. Wang, J.G. Dai, A multiscale study on gel composition of hybrid alkali-activated materials partially utilizing air pollution control residue as an activator, Cement Concrete Comp, 136 (2023) 104856.
[104] M.R. Sadat, S. Bringuier, K. Muralidharan, K. Runge, A. Asaduzzaman, L.Y. Zhang, An atomistic characterization of the interplay between composition, structure and mechanical properties of amorphous geopolymer binders, J Non-Cryst Solids, 434 (2016) 53-61.
[105] X.W. Guan, L. Jiang, D. Fan, A.G. Hernandez, B. Li, H. Do, Molecular simulations of the structure-property relationships of N-A-S-H gels, Constr Build Mater, 329 (2022) 127166.

[106] H.M. Jennings, A model for the microstructure of calcium silicate hydrate in cement paste, Cement Concrete Res, 30 (2000) 101-116.
[107] P. Duxson, J.L. Provis, G.C. Lukey, S.W. Mallicoat, W.M. Kriven, J.S.J. van Deventer, Understanding the relationship between geopolymer composition, microstructure and mechanical properties, Colloid Surface A, 269 (2005) 47-58.
[108] M.U. Kankia, L. Baloo, N. Danlami, N.A. Zawawi, A. Bello, S.I. Muhammad, Microstructural Analysis and Compressive Strength of Fly Ash and Petroleum Sludge Ash Geopolymer Mortar under High Temperatures, Sustainability-Basel, 15 (2023) 9846.
[109] I. Zafar, K. Rashid, R. Hameed, K. Aslam, Correlating Reactivity of Fly Ash with Mechanical Strength of the Resultant Geopolymer, Arab J Sci Eng, 47 (2022) 12469-12478.
[110] C. Kuenzel, N. Ranjbar, Dissolution mechanism of fly ash to quantify the reactive aluminosilicates in geopolymerisation, Resour Conserv Recy, 150 (2019) 104421.
[111] A. Fernández-Jiménez, A. Palomo, M. Criado, Microstructure development of alkali-activated fly ash cement:: a descriptive model, Cement Concrete Res, 35 (2005) 1204-1209.
[112] J.L. Provis, J.S.J. van Deventer, Geopolymerisation kinetics. 2. Reaction kinetic modelling, Chem Eng Sci, 62 (2007) 2318-2329.
[113] J.J. Thomas, H.M. Jennings, A colloidal interpretation of chemical aging of the C-S-H gel and its effects on the properties of cement paste, Cement Concrete Res, 36 (2006) 30-38.
[114] A. Hajimohammadi, J.S.J. van Deventer, Dissolution behaviour of source materials for synthesis of geopolymer binders: A kinetic approach, Int J Miner Process, 153 (2016) 80-86.
[115] R.R. Lloyd, J.L. Provis, J.S.J. van Deventer, Microscopy and microanalysis of inorganic polymer cements. 1: remnant fly ash particles, J Mater Sci, 44 (2009) 608-619.
[116] D.W. Zhang, X.M. Sun, H. Li, Relationship between macro-properties and amorphous gel of FA-based AAMs with different curing conditions after elevated temperature, Ceram Int, 49 (2023) 17453-17467.
[117] M. Criado, A. Fernández-Jiménez, A. Palomo, I. Sobrados, J. Sanz, Effect of the Sio/NaO ratio on the alkali activation of fly ash. Part II: Si MAS-NMR Survey, Micropor Mesopor Mat, 109 (2008) 525-534.
[118] A. Palomo, S. Alonso, A. Femandez-Jiménez, Alkaline activation of fly ashes:: NMR study of the reaction products, J Am Ceram Soc, 87 (2004) 1141-1145.
[119] W.L. Tu, G.H. Fang, B.Q. Dong, M.Z. Zhang, Multiscale study of microstructural evolution in alkali-activated fly ash-slag paste at elevated temperatures, Cement Concrete Comp, 143 (2023) 105258.

[120] M.R. Ahmad, M. Khan, A.G. Wang, Z.H. Zhang, J.G. Dai, Alkali-activated materials partially activated using flue gas residues: An insight into reaction products, Constr Build Mater, 371 (2023) 130760.
[121] Z.Y. Luo, W.G. Li, Y.X. Gan, K. Mendu, S.P. Shah, Applying grid nanoindentation and maximum likelihood estimation for N-A-S-H gel in geopolymer paste: Investigation and discussion, Cement Concrete Res, 135 (2020) 106112.
[122] G.A. Lyngdoh, S. Nayak, N.M.A. Krishnan, S. Das, Fracture toughness of fly ash-based geopolymer gels: Evaluations using nanoindentation experiment and molecular dynamics simulation, Constr Build Mater, 262 (2020) 120797.
[123] R.Z. Si, S.C. Guo, Q.L. Dai, J.Q. Wang, Atomic-structure, microstructure and mechanical properties of glass powder modified metakaolin-based geopolymer, Constr Build Mater, 254 (2020) 119303.
[124] E. Kamseu, A.T. Akono, A. Nana, R.C. Kaze, C. Leonelli, Performance of geopolymer composites made with feldspathic solid solutions: Micromechanics and microstructure, Cement Concrete Comp, 124 (2021) 104241.
[125] Z.Y. Luo, W.G. Li, Y.X. Gan, X.Z. He, A. Castel, D.C. Sheng, Nanoindentation on micromechanical properties and microstructure of geopolymer with nano-SiO and nano-TiO, Cement Concrete Comp, 117 (2021) 103883.
[126] Z.Y. Luo, W.G. Li, P.R. Li, K.J. Wang, S.P. Shah, Investigation on effect of nanosilica dispersion on the properties and microstructures of fly ash-based geopolymer composite, Constr Build Mater, 282 (2021) 122690.
[127] H. Alanazi, Y.R. Kim, J. Hu, D.N. Little, J.S. Jung, Multiscale Characterization of Fly Ash-Based Geopolymer and Type V Portland Cement Exposed to MgSO, J Mater Civil Eng, 34 (2022) 04022095.
[128] P.S. Deb, M.N.N. Khan, P.K. Sarker, S. Barbhuiya, Nanomechanical characterization of ambient-cured fly ash geopolymers containing nanosilica, J Sustain Cem-Based, 11 (2022) 164-174.
[129] M. Lizcano, H.S. Kim, S. Basu, M. Radovic, Mechanical properties of sodium and potassium activated metakaolin-based geopolymers, J Mater Sci, 47 (2012) 2607-2616.
[130] M.R. Sadat, S. Bringuier, A. Asaduzzaman, K. Muralidharan, L. Zhang, A molecular dynamics study of the role of molecular water on the structure and mechanics of amorphous geopolymer binders, J Chem Phys, 145 (2016) 134706.
[131] M. Jin, Y.F. Ma, W.W. Li, J.L. Huang, Y. Yan, H.Y. Zeng, C. Lu, J.P. Liu, Multi-scale investigation on composition-structure of C-(A)-S-H with different Al/Si ratios under attack of decalcification action, Cement Concrete Res, 172 (2023) 107251.

[132] X. Liu, P. Feng, W. Li, G.Q. Geng, J.L. Huang, Y. Gao, S. Mu, J.X. Hong, Effects of pH on the nano/micro structure of calcium silicate hydrate (C-S-H) under sulfate attack, Cement Concrete Res, 140 (2021) 106306.
[133] X. Liu, P. Feng, Y.X. Cai, X.H. Yu, Q. Liu, Carbonation behaviors of calcium silicate hydrate (C-S-H): Effects of aluminum, Constr Build Mater, 325 (2022) 126825.
[134] V. Kanchanason, J. Plank, Role of pH on the structure, composition and morphology of C-S-H-PCE nanocomposites and their effect on early strength development of Portland cement, Cement Concrete Res, 102 (2017) 90-98.
[135] E. L'Hôpital, B. Lothenbach, D.A. Kulik, K. Scrivener, Influence of calcium to silica ratio on aluminium uptake in calcium silicate hydrate, Cement Concrete Res, 85 (2016) 111-121.
[136] A.K. Mohamed, P. Moutzouri, P. Berruyer, B.J. Walder, J. Siramanont, M. Harris, M. Negroni, S.C. Galmarini, S.C. Parker, K.L. Scrivener, L. Emsley, P. Bowen, The Atomic-Level Structure of Cementitious Calcium Aluminate Silicate Hydrate, J Am Chem Soc, 142 (2020) 11060-11071.
[137] E. L'Hopital, B. Lothenbach, G. Le Saout, D. Kulik, K. Scrivener, Incorporation of aluminium in calcium-silicate-hydrates, Cement Concrete Res, 75 (2015) 91-103.
[138] X. Pardal, F. Brunet, T. Charpentier, I. Pochard, A. Nonat, 27Al and 29Si Solid-State NMR Characterization of Calcium Aluminosilicate-Hydrate, Inorg Chem, 51 (2012) 1827-1836.
[139] Y. Yan, G.Q. Geng, Evolution of C-S-H morphology at early age: New insights from direct TEM observation, J Build Eng, 73 (2023) 106764.
[140] E.T. Rodriguez, I.G. Richardson, L. Black, E. Boehm-Courjault, A. Nonat, J. Skibsted, Composition, silicate anion structure and morphology of calcium silicate hydrates (C-S-H) synthesised by silica-lime reaction and by controlled hydration of tricalcium silicate (C3S), Adv Appl Ceram, 114 (2015) 362-371.
[141] Q. Zheng, J.Y. Jiang, X.L. Li, K.C. Bustillo, H.M. Zheng, TEM observation of calcium silicate hydrate nanostructure at high temperatures, Cement Concrete Res, 149 (2021) 106579.
[142] K.Y. Liao, A. Masuno, A. Taguchi, H. Moriwake, H. Inoue, T. Mizoguchi, Revealing Spatial Distribution of Al-Coordinated Species in a Phase-Separated Aluminosilicate Glass by STEM-EELS, J Phys Chem Lett, 11 (2020) 9637-9642.
[143] M. Vandamme, F.J. Ulm, Nanogranular origin of concrete creep, P Natl Acad Sci USA, 106 (2009) 10552-10557.
[144] G. Constantinides, Invariant mechanical properties of calcium-silicate-hydrates (CHS) in cement-based materials: instrumented nanoindentation and microporomechanical modeling, Massachusetts Institute of Technology, 2006.

[145] A. Cuesta, I. Santacruz, A.G. De la Torre, M. Dapiaggi, J.D. Zea-Garcia, M.A.G. Aranda, Local structure and Ca/Si ratio in C-S-H gels from hydration of blends of tricalcium silicate and silica fume, Cement Concrete Res, 143 (2021) 106405.
[146] J. Yang, Q.J. Ding, G.Z. Zhang, D.S. Hou, M.Y. Zhao, J.R. Cao, Effect of sulfate attack on the composition and micro-mechanical properties of C-A-S-H gel in cement-slag paste: A combined study of nanoindentation and SEM-EDS, Constr Build Mater, 345 (2022) 128275.
[147] X.T. Xing, B.H. Wang, H. Liu, S.J. Luo, S.Z. Wang, J.X. Wei, W.T. Xu, Q.J. Yu, The mechanism of silane-grafted sodium polyacrylate on the toughening of slag-based geopolymer: an insight from macroscopic-microscopic mechanical properties, J Mater Sci, 58 (2023) 8757-8778.
[148] J.E. Oh, P.J.M. Monteiro, S.S. Jun, S. Choi, S.M. Clark, The evolution of strength and crystalline phases for alkali-activated ground blast furnace slag and fly ash-based geopolymers, Cement Concrete Res, 40 (2010) 189-196.
[149] X. Chen, G.R. Zhu, J. Wang, Q. Chen, Effect of polyacrylic resin on mechanical properties of granulated blast furnace slag based geopolymer, J Non-Cryst Solids, 481 (2018) 4-9.
[150] B. Mast, S. Fransis, B. Vandoren, A. Cambriani, W. Schroeyers, Y. Pontikes, P. Samyn, S. Schreurs, Micromechanical and microstructural analysis of Fe-rich plasma slag-based inorganic polymers, Cement Concrete Comp, 118 (2021) 103968.
[151] R.L. Cao, Z.J. Jia, S.Q. Zhang, C. Chen, Y.Y. Gao, Y.M. Zhang, Effect of low-calcium and high-magnesium ferronickel slag on the microstructure and micromechanical properties of alkali-activated blended ground granulated blast furnace slag, Constr Build Mater, 406 (2023) 133421.
[152] Z.J. Jia, R.L. Cao, S.Q. Zhang, C. Chen, Y.M. Zhang, Insights into the microstructure and mechanical properties evolution of hydration products in cementitious materials incorporating GGBFS, J Sustain Cem-Based, 12 (2023) 403-414.
[153] I.G. Richardson, S. Li, Composition and structure of an 18-year-old 5M KOH-activated ground granulated blast-furnace slag paste, Constr Build Mater, 168 (2018) 404-411.
[154] A.R. Brough, A. Atkinson, Sodium silicate-based, alkali-activated slag mortars Part I. Strength, hydration and microstructure, Cement Concrete Res, 32 (2002) 865-879.
[155] B.S. Gebregziabiher, R. Thomas, S. Peethamparan, Very early-age reaction kinetics and microstructural development in alkali-activated slag, Cement Concrete Comp, 55 (2015) 91-102.
[156] F. Puertas, A. Fernández-Jiménez, Mineralogical and microstructural characterisation of alkali-activated fly ash/slag pastes, Cement Concrete Comp, 25 (2003) 287-292.
[157] Z.J. Jia, C. Chen, H.Y. Zhou, Y.M. Zhang, The characteristics and formation mechanism of the dark rim in alkali-activated slag, Cement Concrete Comp, 112 (2020) 103682.

[158] U. Javed, F.U.A. Shaikh, P.K. Sarker, A comprehensive micro-nano investigative approach to study the development of aluminosilicate gel in binary blends of lithium slag geopolymer, Cement Concrete Comp, 145 (2024) 105338.
[159] N. Marjanovic, M. Komljenovic, Z. Bascarevic, V. Nikolic, R. Petrovic, Physical-mechanical and microstructural properties of alkali-activated fly ash-blast furnace slag blends, Ceram Int, 41 (2015) 1421-1435.
[160] P.T. Durdzinski, C.F. Dunant, M. Ben Haha, K.L. Scrivener, A new quantification method based on SEM-EDS to assess fly ash composition and study the reaction of its individual components in hydrating cement paste, Cement Concrete Res, 73 (2015) 111-122.
[161] S. Puligilla, P. Mondal, Role of slag in microstructural development and hardening of fly ash-slag geopolymer, Cement Concrete Res, 43 (2013) 70-80.
[162] S. Bae, C. Meral, J.E. Oh, J. Moon, M. Kunz, P.J.M. Monteiro, Characterization of morphology and hydration products of high-volume fly ash paste by monochromatic scanning x-ray micro-diffraction (μ-SXRD), Cement Concrete Res, 59 (2014) 155-164.
[163] G.H. Fang, Q. Wang, M.Z. Zhang, In-situ X-ray tomographic imaging of microstructure evolution of fly ash and slag particles in alkali-activated fly ash-slag paste, Compos Part B-Eng, 224 (2021) 109221.
[164] T.H.Y. Nguyen, K. Tsuchiya, D. Atarashi, Microstructure and composition of fly ash and ground granulated blast furnace slag cement pastes in 42-month cured samples, Constr Build Mater, 191 (2018) 114-124.
[165] L. Wang, B. Yang, A. Abraham, L. Qi, X.Y. Zhao, Z.X. Chen, Construction of dynamic three-dimensional microstructure for the hydration of cement using 3D image registration, Pattern Anal Appl, 17 (2014) 655-665.
[166] M.Z. Zhang, Pore-scale modelling of relative permeability of cementitious materials using X-ray computed microtomography images, Cement Concrete Res, 95 (2017) 18-29.
[167] J. Adrien, S. Meille, S. Tadier, E. Maire, L. Sasaki, X-ray tomographic monitoring of gypsum plaster setting, Cement Concrete Res, 82 (2016) 107-116.
[168] R.T. Chancey, P. Stutzman, M.C.G. Juenger, D.W. Fowler, Comprehensive phase characterization of crystalline and amorphous phases of a Class F fly ash, Cement Concrete Res, 40 (2010) 146-156.
[169] F. Puertas, M. Palacios, H. Manzano, J.S. Dolado, A. Rico, J. Rodríguez, A model for the C-A-S-H gel formed in alkali-activated slag cements, J Eur Ceram Soc, 31 (2011) 2043-2056.
[170] M. Nedeljkovic, B. Savija, Y.B. Zuo, M. Lukovic, G. Ye, Effect of natural carbonation on the pore structure and elastic modulus of the alkali-activated fly ash and slag pastes, Constr Build Mater, 161 (2018) 687-704.

[171] Y. Luo, H.J.H. Brouwers, Q.L. Yu, Understanding the gel compatibility and thermal behavior of alkali activated Class F fly ash/ladle slag: The underlying role of Ca availability, Cement Concrete Res, 170 (2023) 107198.
[172] I. García-Lodeiro, A. Fernández-Jiménez, A. Palomo, Variation in hybrid cements over time. Alkaline activation of fly ash-portland cement blends, Cement Concrete Res, 52 (2013) 112-122.
[173] I. García-Lodeiro, A. Fernández-Jiménez, A. Palomo, D.E. Macphee, Effect of Calcium Additions on N-A-S-H Cementitious Gels, J Am Ceram Soc, 93 (2010) 1934-1940.
[174] J.S.J. van Deventer, R.S. Nicolas, I. Ismail, S.A. Bernal, D.G. Brice, J.L. Provis, Microstructure and durability of alkali-activated materials as key parameters for standardization, J Sustain Cem-Based, 4 (2015) 116-128.
[175] M. Elzeadani, D.V. Bompa, A.Y. Elghazouli, One part alkali activated materials: A state-of-the-art review, J Build Eng, 57 (2022) 104871.
[176] H.Y. Zhang, J.C. Liu, B. Wu, Mechanical properties and reaction mechanism of one-part geopolymer mortars, Constr Build Mater, 273 (2021) 121973.
[177] S.B. Zhou, C. Ma, G.C. Long, Y.J. Xie, A novel non-Portland cementitious material: Mechanical properties, durability and characterization, Constr Build Mater, 238 (2020) 117671.
[178] S.L. Guo, C. Ma, G.C. Long, Y.J. Xie, Cleaner one-part geopolymer prepared by introducing fly ash sinking spherical beads: Properties and geopolymerization mechanism, J Clean Prod, 219 (2019) 686-697.
[179] A. Dakhane, N. Neithalath, Reaction kinetics and characterization of slag-based, high strength,“just-add-water” type (one-part) alkali-activated binders, Recent Progress in Materials, 4 (2022) 1-21.
[180] I. García-Lodeiro, O. Maltseva, A. Palomo, A. Fernández-Jiménez, Hybrid Alkaline Cements. Part I: Fundamentals, Rev Rom Mater, 42 (2012) 330-335.
[181] A. Keulen, Q.L. Yu, S. Zhang, S. Grünewald, Effect of admixture on the pore structure refinement and enhanced performance of alkali-activated fly ash-slag concrete, Constr Build Mater, 162 (2018) 27-36.
[182] S.K. Chen, S.Q. Ruan, Q. Zeng, Y. Liu, M.Z. Zhang, Y. Tian, D.M. Yan, Pore structure of geopolymer materials and its correlations to engineering properties: A review, Constr Build Mater, 328 (2022) 127064.
[183] D.M. Yan, S.K. Chen, Q. Zeng, S.L. Xu, H.D. Li, Correlating the elastic properties of metakaolin-based geopolymer with its composition, Mater Design, 95 (2016) 306-318.
[184] T. Yang, H.J. Zhu, Z.H. Zhang, Influence of fly ash on the pore structure and shrinkage characteristics of metakaolin-based geopolymer pastes and mortars, Constr Build Mater, 153 (2017) 284-293.

[185] J.L. Provis, R.J. Myers, C.E. White, V. Rose, J.S.J. van Deventer, X-ray microtomography shows pore structure and tortuosity in alkali-activated binders, Cement Concrete Res, 42 (2012) 855-864.
[186] P. Duan, C.J. Yan, W. Zhou, W.J. Luo, C.H. Shen, An investigation of the microstructure and durability of a fluidized bed fly ash-metakaolin geopolymer after heat and acid exposure, Mater Design, 74 (2015) 125-137.
[187] D.L. Kong, J.G. Sanjayan, K. Sagoe-Crentsil, Comparative performance of geopolymers made with metakaolin and fly ash after exposure to elevated temperatures, Cement Concrete Res, 37 (2007) 1583-1589.
[188] Z.H. Zhang, J.L. Provis, A. Reid, H. Wang, Fly ash-based geopolymers: The relationship between composition, pore structure and efflorescence, Cement Concrete Res, 64 (2014) 30-41.
[189] D. Ravikumar, S. Peethamparan, N. Neithalath, Structure and strength of NaOH activated concretes containing fly ash or GGBFS as the sole binder, Cement Concrete Comp, 32 (2010) 399-410.
[190] Y. Luo, K.M. Klima, H.J.H. Brouwers, Q.L. Yu, Effects of ladle slag on Class F fly ash geopolymer: Reaction mechanism and high temperature behavior, Cement Concrete Comp, 129 (2022) 104468.
[191] S.M. Park, J.G. Jang, N.K. Lee, H.K. Lee, Physicochemical properties of binder gel in alkali-activated fly ash/slag exposed to high temperatures, Cement Concrete Res, 89 (2016) 72-79.
[192] Y. Li, K.H. Tan, E.H. Yang, Synergistic effects of hybrid polypropylene and steel fibers on explosive spalling prevention of ultra-high performance concrete at elevated temperature, Cement Concrete Comp, 96 (2019) 174-181.
[193] M. Nedeljkovic, K. Arbi, Y. Zuo, G. Ye, Microstructural and mineralogical analysis of alkali activated fly ash-slag pastes, Microdurability 2016: the International Rilem Conference on Microstructure Related Durability of Cementitious Composites, 2016.
[194] M. Ben Haha, B. Lothenbach, G. Le Saout, F. Winnefeld, Influence of slag chemistry on the hydration of alkali-activated blast-furnace slag - Part I: Effect of MgO, Cement Concrete Res, 41 (2011) 955-963.
[195] X. Liu, S. Nair, K. Aughenbaugh, E. van Oort, Mud-to-cement conversion of non-aqueous drilling fluids using alkali-activated fly ash, Journal of Petroleum Science and Engineering, 182 (2019) 106242.
[196] R.N. Thakur, S. Ghosh, Effect of mix composition on compressive strength and microstructure of fly ash based geopolymer composites, ARPN J. Eng. Appl. Sci, 4 (2009) 68-74.

[197] M.N.S. Hadi, H.Q. Zhang, S. Parkinson, Optimum mix design of geopolymer pastes and concretes cured in ambient condition based on compressive strength, setting time and workability, J Build Eng, 23 (2019) 301-313.
[198] X. Yao, T. Yang, Z.H. Zhang, Compressive strength development and shrinkage of alkali-activated fly ash-slag blends associated with efflorescence, Mater Struct, 49 (2016) 2907-2918.
[199] M. Chi, Y. Liu, R. Huang, Mechanical and microstructural characterization of alkali-activated materials based on fly ash and slag, International Journal of Engineering and Technology, 7 (2015) 59.
[200] X.W. Ouyang, Y.W. Ma, Z.Y. Liu, J.J. Liang, G. Ye, Effect of the Sodium Silicate Modulus and Slag Content on Fresh and Hardened Properties of Alkali-Activated Fly Ash/Slag, Minerals-Basel, 10 (2020) 15.
[201] S.Q. Ruan, Y.L. Qiu, R.F. Gao, S.K. Chen, H. Qian, Y. Liu, D.M. Yan, Effect of organosilicone on the reaction process of functionalized geopolymers, J Build Eng, 76 (2023) 107348.
[202] A.M. Rashad, Performance of autoclaved alkali-activated metakaolin pastes blended with micro-size particles derivative from dehydroxylation of kaolinite, Constr Build Mater, 248 (2020) 118671.
[203] A.M. Rashad, A.S. Ouda, D.M. Sadek, Behavior of Alkali-Activated Metakaolin Pastes Blended with Quartz Powder Exposed to Seawater Attack, J Mater Civil Eng, 30 (2018) 04018159.
[204] W.L. Tu, Y. Zhu, G.H. Fang, X.G. Wang, M.Z. Zhang, Internal curing of alkali-activated fly ash-slag pastes using superabsorbent polymer, Cement Concrete Res, 116 (2019) 179-190.
[205] W. Zhang, X. Yao, T. Yang, C. Liu, Z.H. Zhang, Increasing mechanical strength and acid resistance of geopolymers by incorporating different siliceous materials, Constr Build Mater, 175 (2018) 411-421.
[206] M. Nili, A. Ehsani, Investigating the effect of the cement paste and transition zone on strength development of concrete containing nanosilica and silica fume, Mater Design, 75 (2015) 174-183.
[207] J.P. Ollivier, J.C. Maso, B. Bourdette, Interfacial Transition Zone in Concrete, Adv Cem Based Mater, 2 (1995) 30-38.
[208] A. Bentur, M.G. Alexander, R.T. Comm, A review of the work of the RILEM TC 159-ETC: Engineering of the interfacial transition zone in cementitious composites, Mater Struct, 33 (2000) 82-87.
[209] K.L. Scrivener, A.K. Crumbie, P. Laugesen, The interfacial transition zone (ITZ) between cement paste and aggregate in concrete, Interface Sci, 12 (2004) 411-421.
[210] Z.Y. Luo, W.G. Li, K.J. Wang, A. Castel, S.P. Shah, Comparison on the properties of ITZs in fly ash-based geopolymer and Portland cement concretes with equivalent flowability, Cement Concrete Res, 143 (2021) 106392.

[211] H.S. Wong, M. Zobel, N.R. Buenfeld, R.W. Zimmerman, Influence of the interfacial transition zone and microcracking on the diffusivity, permeability and sorptivity of cement-based materials after drying, Mag Concrete Res, 61 (2009) 571-589.
[212] Z.Y. Luo, W.G. Li, K.J. Wang, S.P. Shah, D.C. Sheng, Nano/micromechanical characterisation and image analysis on the properties and heterogeneity of ITZs in geopolymer concrete, Cement Concrete Res, 152 (2022) 106677.
[213] W.G. Li, Z.Y. Luo, Y.X. Gan, K.J. Wang, S.P. Shah, Nanoscratch on mechanical properties of interfacial transition zones (ITZs) in fly ash-based geopolymer composites, Compos Sci Technol, 214 (2021) 109001.
[214] J.L. Provis, G.C. Lukey, J.S.J. van Deventer, Do geopolymers actually contain nanocrystalline zeolites? A reexamination of existing results, Chem Mater, 17 (2005) 3075-3085.
[215] Z.Y. Luo, W.G. Li, Y.X. Gan, K. Mendu, S.P. Shah, Maximum likelihood estimation for nanoindentation on sodium aluminosilicate hydrate gel of geopolymer under different silica modulus and curing conditions, Compos Part B-Eng, 198 (2020) 108185.
[216] P.G. Allison, C.A. Weiss, R.D. Moser, A.J. Diaz, O.G. Rivera, S.S. Holton, Nanoindentation and SEM/EDX characterization of the geopolymer-to-steel interfacial transition zone for a reactive porcelain enamel coating, Compos Part B-Eng, 78 (2015) 131-137.
[217] M. Khedmati, Y.R. Kim, J.A. Turner, H. Alanazi, C. Nguyen, An integrated microstructural-nanomechanical-chemical approach to examine material-specific characteristics of cementitious interphase regions, Mater Charact, 138 (2018) 154-164.
[218] M. Khedmati, Y.R. Kim, J.A. Turner, Investigation of the interphase between recycled aggregates and cementitious binding materials using integrated microstructural-nanomechanical-chemical characterization, Compos Part B-Eng, 158 (2019) 218-229.
[219] H. Peng, C. Cui, C.S. Cai, Y. Liu, Z. Liu, Microstructure and microhardness property of the interface between a metakaolin/GGBFS-based geopolymer paste and granite aggregate, Constr Build Mater, 221 (2019) 263-273.
[220] C. Shi, P. Xie, Interface between cement paste and quartz sand in alkali-activated slag mortars, Cement Concrete Res, 28 (1998) 887-896.
[221] Y. Ding, J.G. Dai, C.J. Shi, Fracture properties of alkali-activated slag and ordinary Portland cement concrete and mortar, Constr Build Mater, 165 (2018) 310-320.
[222] Z.Y. Luo, W.G. Li, K.J. Wang, S.P. Shah, Research progress in advanced nanomechanical characterization of cement-based materials, Cement Concrete Comp, 94 (2018) 277-295.
[223] W.K.W. Lee, J.S.J. van Deventer, The interface between natural siliceous aggregates and geopolymers, Cement Concrete Res, 34 (2004) 195-206.

[224] T. Ji, Q. Gao, W. Zheng, X. Lin, H.-C. Wu, Interfacial transition zone of alkali-activated slag concrete, Aci Mater J, 114 (2017) 347.
[225] S.A. Bernal, R.M. de Gutiérrez, A.L. Pedraza, J.L. Provis, E.D. Rodriguez, S. Delvasto, Effect of binder content on the performance of alkali-activated slag concretes, Cement Concrete Res, 41 (2011) 1-8.
[226] G.H. Fang, Q. Wang, M.Z. Zhang, Micromechanical analysis of interfacial transition zone in alkali-activated fly ash-slag concrete, Cement Concrete Comp, 119 (2021) 103990.
[227] R.L. Cao, S.Q. Zhang, N. Banthia, Y.M. Zhang, Z.H. Zhang, Interpreting the early-age reaction process of alkali-activated slag by using combined embedded ultrasonic measurement, thermal analysis, XRD, FTIR and SEM, Compos Part B-Eng, 186 (2020) 107840.
[228] S.K. Nath, S. Kumar, Reaction kinetics, microstructure and strength behavior of alkali activated silico-manganese (SiMn) slag - Fly ash blends, Constr Build Mater, 147 (2017) 371-379.
[229] Y. Jin, D. Stephan, The unusual solidification process of alkali activated slag and its relationship with the glass structure of the slag, Cement Concrete Res, 121 (2019) 1-10.
[230] L.J. Kong, Z.R. Fan, J.T. Lu, L.Y. Zhang, Microstructure evolution of interfacial transition zone between alkali-activated fly ash/slag matrix and aggregate, Mater Struct, 55 (2022) 203.
[231] A.W. Pope, H.M. Jennings, The Influence of Mixing on the Microstructure of the Cement Paste Aggregate Interfacial Zone and on the Strength of Mortar, J Mater Sci, 27 (1992) 6452-6462.
[232] R.S. Nicolas, J.L. Provis, The Interfacial Transition Zone in Alkali-Activated Slag Mortars, Front Mater, 2 (2015) 70.
[233] J.A. Larbi, J.M.J.M. Bijen, Effects of Water-Cement Ratio, Quantity and Fineness of Sand on the Evolution of Lime in Set Portland-Cement Systems, Cement Concrete Res, 20 (1990) 783-794.
[234] A. Hassan, M. Arif, M. Shariq, Use of geopolymer concrete for a cleaner and sustainable environment - A review of mechanical properties and microstructure, J Clean Prod, 223 (2019) 704-728.
[235] S.K. John, Y. Nadir, K. Girija, Effect of source materials, additives on the mechanical properties and durability of fly ash and fly ash-slag geopolymer mortar: A review, Constr Build Mater, 280 (2021) 122443.
[236] A.S. Albidah, Effect of partial replacement of geopolymer binder materials on the fresh and mechanical properties: A review, Ceram Int, 47 (2021) 14923-14943.
[237] P. Chindasiriphan, P. Nuaklong, S. Keawsawasvong, C. Thongchom, T. Jirawattanasomkul, P. Jongvivatsakul, W. Tangchirapat, S. Likitlersuang, Effect of superabsorbent polymer and polypropylene fiber on mechanical performances of alkali-activated high-calcium fly ash mortar under ambient and elevated temperatures, J Build Eng, 71 (2023) 106509.

[238] L.J. Kong, Z.R. Fan, W.C. Ma, J.T. Lu, Y.Z. Liu, Effect of Curing Conditions on the Strength Development of Alkali-Activated Mortar, Crystals, 11 (2021) 1455.
[239] H. Rashidian-Dezfouli, P.R. Rangaraju, V.S.K. Kothala, Influence of selected parameters on compressive strength of geopolymer produced from ground glass fiber, Constr Build Mater, 162 (2018) 393-405.
[240] M.C. Chi, R. Huang, Binding mechanism and properties of alkali-activated fly ash/slag mortars, Constr Build Mater, 40 (2013) 291-298.
[241] P. Nuaklong, K. Hamcumpai, S. Keawsawasvong, S. Pethrung, P. Jongvivatsakul, S. Tangaramvong, T. Pothisiri, S. Likitlersuang, Strength and post-fire performance of fiber-reinforced alkali-activated fly ash concrete containing granite industry waste, Constr Build Mater, 392 (2023) 131984.
[242] G. Nagalia, Y. Park, A. Abolmaali, P. Aswath, Compressive strength and microstructural properties of fly ash–based geopolymer concrete, J Mater Civil Eng, 28 (2016) 04016144.
[243] S.J. Chithambaram, S. Kumar, M.M. Prasad, D. Adak, Effect of parameters on the compressive strength of fly ash based geopolymer concrete, Struct Concrete, 19 (2018) 1202-1209.
[244] A. Esparham, A.B. Moradikhou, Factors influencing compressive strength of fly ash-based geopolymer concrete, Amirkabir Journal of Civil Engineering, 53 (2021) 21-31.
[245] A. Kalaiyarrasi, P. Partheeban, Influence of Si/Al ratio on the compressive strength of metakaolin based geopolymers, International Journal of Earth sciences and Engineering, (2016) 87-91.
[246] M.C. Chi, Mechnical Strength and Durability of Alkali-Activated Fly Ash/Slag Concrete, J Mar Sci Tech-Taiw, 24 (2016) 958-967.
[247] S. Divvala, Early strength properties of geopolymer concrete composites: An experimental study, Materials Today: Proceedings, 47 (2021) 3770-3777.
[248] Y.R. Alharbi, A.A. Abadel, A.A. Salah, O.A. Mayhoub, M. Kohail, Engineering properties of alkali activated materials reactive powder concrete, Constr Build Mater, 271 (2021) 121550.
[249] H.G. Zhang, L. Li, C. Yuan, Q.Y. Wang, P.K. Sarker, X.S. Shi, Deterioration of ambient-cured and heat-cured fly ash geopolymer concrete by high temperature exposure and prediction of its residual compressive strength, Constr Build Mater, 262 (2020) 120924.
[250] A. Hassan, M. Arif, M. Shariq, Mechanical Behaviour and Microstructural Investigation of Geopolymer Concrete After Exposure to Elevated Temperatures, Arab J Sci Eng, 45 (2020) 3843-3861.
[251] R. He, N. Dai, Z.J. Wang, Thermal and Mechanical Properties of Geopolymers Exposed to High Temperature: A Literature Review, Adv Civ Eng, 2020 (2020) 1-17.